LINEAR ELASTIC RESPONSE OF TUBES TO INTERNAL DETONATION LOADING

W.M. Beltman

University of Twente, Department of Mechanical Engineering,

P.O. Box 217, 7500 AE Enschede, The Netherlands

J.E. Shepherd

California Institute of Technology, Graduate Aeronautical Laboratories,

Pasadena, CA 91125, U.S.A.

Total number of pages: 60

Total number of figures: 20

Total number of tables: 4

Total number of footnotes: 4

Postal address and address for proofs:

Prof. Joseph E. Shepherd

Aeronautics, MS 105-50

California Institute of Technology

Pasadena, CA 91125 USA

Phone: (626) 395 3283

Fax: (626) 449 2677

E-mail: jeshep@galcit.caltech.edu

SUMMARY

This paper deals with the structural response of a tube to an internal gaseous detonation. An internal detonation produces a pressure load that propagates down the tube. Because the speed of the gaseous detonation can be comparable to the flexural wave group speed, excitation of flexural waves in the tube wall must be considered. Flexural waves can result in much higher strains and stresses than static loading with the same loading pressures. Experiments and numerical simulations were used to determine the structural response. In the experiments, a detonation tube was instrumented with a number of strain gages. A series of experiments was carried out under different conditions. Strains were measured that exceed the equivalent static strain by up to a factor of 3.9. Special attention was paid to the influence of the detonation speed, reflection and interference of structural waves at flanges and also at the tube end, the linearity of the response, the transient development of the deflection profile, and the influence of detonation cell size. Analytical models and finite element models were used to interpret the observations and to make quantitative predictions of the peak strain.

2

1 INTRODUCTION

1.1 DETONATIONS AND STRUCTURES

A common experimental technique and situation encountered in accidental explosion analyses is a detonation wave propagating within a tube or pipe. From a structural point of view, the tube experiences a traveling internal load that produces transient deformation of the tube. This situation is similar to the case of a gaseous shock wave propagating in a tube [1] but with a more complex spatial (Figure 1) and temporal (Figure 2) variation of internal pressure than the simple step function that can be used to represent a shock wave.

In this paper, we consider the elastic response of a tube to the loading resulting from a detonation wave propagating along the axis of the tube starting from the closed end. We carry out calculations using model loading profiles and also report experimental measurements of strain produced in a tube for a range of detonation parameters. We examine the role of spatially nonuniform loading, detonation cellular structure, and the connections between the segments of the tube. This work is closely related to our previous studies [1] of a shock wave propagating in a tube. As in that case, it is

possible to excite flexural waves in the tube wall that may result in much higher strains than are possible under static loading conditions with the same internal pressure. These high strains can be created by several mechanisms, including resonant excitation by a detonation wave traveling near critical speed, the interaction of direct and reflected flexural waves, and coupling between the detonation pressure oscillations and flexural waves that have comparable spatial wavelengths.

1.2 PRESSURE LOADING

A detonation [2] consists of a shock wave and a reaction zone that are tightly coupled. An ideal detonation travels at a nearly constant speed close to the theoretical or Chapman-Jouguet (CJ) velocity v_{cj}, which is between 1500 and 3000 m/s in gases depending on the fuel-oxidizer combination. The reaction zone in a detonation is usually very thin, less than 10 mm for most stoichiometric fuel-air mixtures and less than 100 μm for stoichiometric fuel-oxygen mixtures. Within this reaction zone, temperature, pressure and other properties change rapidly while just downstream of the reaction zone, a much slower variation occurs due to the gas dynamics of the wave propagation process. The pressure just behind the detonation can be as high as 20 to

30 times the ambient pressure. A typical experimental pressure-time trace for a detonation propagating longitudinally from the closed end of a tube is shown in Figure 2.

The almost instantaneous jump in pressure at time 0 corresponds to the passage of the detonation wave past the measuring station. The rapid decrease in pressure in the first .01 ms is associated with the reaction zone. The more gradual decrease in pressure out to 0.25 ms and plateau for longer times is associated with the gas dynamics of the flow behind the wave. Superimposed on the general trend are pressure fluctuations due to the unstable nature of the coupling between chemical kinetics and the leading shock front. These pressure fluctuations are indicative of the system of weak transverse shock waves that are well known and characteristic of all gaseous detonations.

In terms of a structural load, the effect is to produce a spatially nonuniform propagating load as shown in Figure 1. Experimental pressure traces and gas dynamic models can be used to define an idealized loading profile. For a tube with a closed end, the situation can be characterized by different regions (see Figure 1). First, there is the initial mixture ahead of the detonation front. The detonation front consists of the shock wave and reaction zone. The detonation is followed by an expansion wave. Behind the expan-

sion wave the gas is stationary. The pressure distribution in such a tube can be described with the Taylor-Zeldovich model [3, 4] as discussed in Appendix B. The profile evolves in a self-similar fashion (the similarity parameter is $x/v_{cj}t$) with the leading pressure wave propagating at the Chapman-Jouguet detonation velocity v_{cj}.

This idealized solution will be used as the basis for our model loading distribution in the computations of structural response. The pressure profile in the expansion wave is given by a power law in the similarity parameter. For simplicity, it is approximated with an exponential decay (see Figure 2 and Appendix B). The model pressure profile is characterized by the velocity v, the initial pressure p_1, the peak pressure p_2, the final pressure p_3, and the exponential decay factor T. The characteristic decay time increases linearly with distance (see Appendix B). Thus, if the detonation is initiated near the closed end on the left, the decay will initially be very sharp. As the detonation progresses, the decay rate decreases. This effect will be addressed in more detail in section 6.6.

In addition to the main pressure loading shown in Figure 1, idealized models [2] predict the existence of a pressure peak (Von Neumann spike) at the front of the reaction zone with a value approximately double that of the

Chapman-Jouguet pressure. This pressure spike is usually not resolved in experiments because of its localized nature and short duration. Since the reaction zone is of such a short length compared to a typical tube length, the influence on the structural response is small in comparison with the effects of the main loading produced by the Taylor-Zeldovich pressure profile behind the detonation front. For these reasons, we have not considered the influence of the Von Neumann pressure spike on the structural response in our numerical models.

We have considered the effect of the reaction zone in our experimental measurements. The unsteady interaction between the chemical reaction and the flow results [2] in a cellular structure that can be observed when a soot foil is inserted in the tube. This structure is a consequence of the detonation front being three dimensional, consisting of weaker shock waves propagating transversely to the main front. The cell size is a characteristic of a particular fuel type, oxidizer and also the amount of diluent (see also Section 5.5). We have examined the effect of the reaction zone by measuring structural response as a function of the characteristic cellular structure width.

1.3   STRUCTURAL RESPONSE

Figure 3 shows the measured circumferential strain as a function of time for a tube with internal detonation loading. The strain history shows a sharp peak when the detonation passes (in this case, at approximately t=2.9 ms). For detonation loading, the circumferential strain can exceed the equivalent static strain by up to a factor of 3 to 4. In the case shown in Figure 3, the peak strain is about 0.8×10^{-4}, a factor of about 1.6 higher than the equivalent static strain computed from equation (2) and the calculated Chapman-Jouguet pressure of 1.7 MPa for this case. This indicates that a simple static model of the tube cross–section is not sufficient. More sophisticated models described subsequently in Sections 2 and 3 take into account the traveling step character of the loading and are able to better reproduce the observed strains. However, real tubes have a finite length, may be made of segments clamped together, and attached to some sort of support structure. In order to make realistic predictions of the structural response of tubes with these features, it is necessary to carry out numerical simulations as discussed subsequently in Section 4.

There have been several investigations dealing with the structural response of shells to internal shock or detonation loading. The simplest dynam-

ical model describes the radial (breathing) motion of the tube cross-section. De Malherbe et al. [5] compared the results of this model to experimental values for detonation loading. Shepherd [6] used the cross-sectional model to predict the response of a tube to internal detonation loading. Van de Ven et al. [7] analysed the response of a tube to an internal dust detonation with a non-rotatory symmetric pressure loading. They present dynamic amplification factors derived from experimentally determined strains. Sperber et al. [8] measured strains produced in a thick wall tube by an acetylene decomposition detonation. They noted that the peak strains were underpredicted by a factor of up to 4 when static formulas were used to estimate the maximum deformation.

Experiments on gun tubes [9, 10] revealed that the propagation speed of the load is an important parameter. Peak strain amplitudes up to three times higher than those predicted by the static Lamé formula were observed when the propagation speed of the load approached a critical value. Further investigation [9, 11, 12] showed that the radial motion created by the traveling load was being resonantly coupled into flexural waves when the load propagation velocity approached the flexural wave group speed. More recently, Beltman et al. [1] observed the same effect in an experimental and

analytical investigation into the structural response of a thin shell to internal shock loading.

The existence of a critical velocity and the potential for resonance effects was first recognized in the investigation of the response of railroad tracks and bridges to the passage of a train or other heavy load. That physical situation can be modeled as a beam on an elastic foundation with a moving load, which results in a governing equation that is identical to the simplest thin-cylinder model of a shock or detonation wave in a tube. The first comprehensive theories for predicting the elastic response of a tube to a moving load were developed by Tang [13] and Reismann [14].

Tang [13] presented a model to predict the response of a thin shell to internal shock loading. By assuming a tube of infinite length, the problem reduces to a "steady state" problem and an analytical solution for the shell motion can be obtained. This type of analytical model will be referred to as the analytical "steady state" model in the present paper. This model predicts the existence of a so-called critical velocity. When the pressure load travels at this critical speed, the solution for the radial tube motion becomes unbounded. Evidently, damping, non-linearities, and plastic deformation will be the controlling mechanisms in this case. Nevertheless, the model is able

to predict the high strains that were found in the experiments. The model presented by Tang includes the effects of rotatory inertia and transverse shear. He also presented transient results for a finite length shell using the method of characteristics. Reismann [14] developed a model that includes the effect of prestress on the structural response and gave an elegant explanation of how the resonant coupling between a moving load and the flexural waves comes about. Simkins [9, 10, 11] extended the analysis to thick-wall tubes and first applied these ideas to explain observations of large strain amplitudes in gun tubes.

1.4 AMPLIFICATION FACTOR

Static pressure vessel design starts by considering the deflections that will be produced by a given internal pressure. Under dynamic loading conditions, the actual deflections will be further amplified by the response of the structure to a time-dependent load. Therefore, an important factor in design for dynamic loading is the amplification factor which is defined as the ratio of the maximum strain to the static strain for the same nominal loading pressure; in this case, the Chapman-Jouguet pressure. The amplification factor is also referred to as the dynamic load factor. In the present work, we measure the

circumferential strain ϵ_θ and infer the radial displacement $w = R\epsilon_\theta$.

In terms of the radial displacement w, the amplification factor is

$$\text{Amplification} = \frac{w_{max}}{w_{static}} \, .$$

(1)

The static strain can be calculated from the time-independent version of the governing equations (see Section 2.1). The maximum static strain for a thin-walled cylinder is

$$\frac{w_{static}}{R} = \frac{R}{h}\frac{\Delta p}{E} \, ,$$

(2)

where the pressure difference $\Delta p = p_{cj} - p_{atm}$ is based on the computed value of the Chapman-Jouguet pressure of the detonation rather than the measured peak pressure. The measured pressure signals are used only in the present investigation to determine the speed of the detonation (see also Section 5.4). One of the goals of the present study is to determine the range of values for the amplification factor under conditions of detonation loading. For simple structures that can be described with a single degree of vibrational freedom, the highest value that the amplification factor can assume is 2. However, for a continuous structure with a traveling load, no such simple estimate appears to be possible and more detailed considerations are needed.

12

2 ANALYTICAL "STEADY STATE" MODEL

The analytical model presented in this section was first developed by Tang [13], who applied it to the case of shock loading. Tang's model is based on a thin shell approximation and includes the effects of rotary inertia and transverse shear deformation but neglects the effect of axial prestress. For a detailed discussion on the influence of the axial prestress, the reader is referred to Reismann [14].

The basic governing equations and solution for the case of steadily propagating detonation in a very long tube are given in this section. The model is steady-state in the sense that the transient development of the tube deformation is ignored and the response is assumed to be time-independent in the frame of reference of the detonation front. The advantages of the steady-state model are that it enables an analytical solution for the deformation, the solution exhibits the excitation of flexural waves, and the existence of a critical speed is clearly shown. The disadvantages are that the response is obviously unrealistic (unbounded) at the critical speed and that features of real tubes such as finite length, supports, or flanges cannot be handled. The

limitations of the steady-state model are addressed in the subsequent section

on the transient analytical model and the finite element solution.

2.1 BASIC EQUATIONS

The basic equations are

$$\frac{\partial N_{xx}}{\partial x} = \rho h \frac{\partial^2 u}{\partial t^2} \, , \qquad \frac{\partial M_{xx}}{\partial x} - Q_x = \rho h^3 \frac{\partial^2 \psi}{\partial t^2} \, ,$$

$$\frac{\partial Q_x}{\partial x} - \frac{N_{\theta\theta}}{R} + \Delta p = \rho h \frac{\partial^2 w}{\partial t^2} \, . \qquad (3)$$

The stress resultants N_{xx}, $N_{\theta\theta}$, M_{xx} and Q_x are defined as:

$$N_{xx} = \frac{Eh}{1 - \nu^2} \left[\frac{\partial u}{\partial x} + \nu \frac{w}{R} \right] \, , \qquad M_{xx} = \frac{Eh^3}{12 \left(1 - \nu^2 \right)} \frac{\partial \psi}{\partial x} \, ,$$

$$N_{\theta\theta} = \frac{Eh}{1 - \nu^2} \left[\nu \frac{\partial u}{\partial x} + \frac{w}{R} \right] \, , \qquad Q_x = \kappa Gh \left[\psi + \frac{\partial w}{\partial x} \right] \, , \qquad (4)$$

where u is the axial displacement, w is the radial displacement, R is the

mean shell radius, h is the shell thickness, t refers to time, ρ is the density

of the shell material, ν is Poisson's ratio, E is Young's modulus, Δp is the

difference between the internal and external pressure, ψ is the rotation, and

κ is the shear correction factor. By demanding that waves with very small

wave numbers propagate at the speed of Rayleigh waves, the value of κ is

determined.

14

Dimensionless quantitities are introduced

$$\overline{u} = \frac{u}{h} \,, \qquad \overline{w} = \frac{w}{h} \,, \quad \overline{\psi} = \frac{1}{\sqrt{12}}\psi \,, \qquad \overline{\eta} = \frac{\sqrt{12}}{h}\left[x - vt\right] \,. \qquad (5)$$

The following parameters are used in the analysis

$$\Lambda_j \;=\; \frac{(p_j - p_{atm})\,R^2}{Eh^2} \quad \text{excitation parameters } (j = 1, 2 \text{ or } 3) \,,$$

$$v_d \;=\; \sqrt{\frac{E}{\rho\,(1 - \nu^2)}} \qquad \text{dilatational wave velocity} \,,$$

$$(6)$$

$$v_s \;=\; \sqrt{\frac{\kappa G}{\rho}} \qquad\qquad \text{shear wave velocity} \,,$$

$$\beta \;=\; \frac{h}{\sqrt{12}R} \qquad\qquad \text{shell thickness parameter} \,.$$

The axial displacement $\overline{u}$ is eliminated by using the first relation in equation

(3). The radial displacement $\overline{w}$ is split up into two contributions

$$\overline{w} = \overline{w}_b + \overline{w}_s \,, \qquad \overline{\psi} = -\frac{\partial \overline{w}_b}{\partial \overline{\eta}} \,. \qquad (7)$$

Inserting these expressions into the equations (3) and (4) and integrating

with respect to $\overline{\eta}$ gives

$$\overline{w}_s = -\left(\frac{v_d}{v_s}\right)^2 \left[1 - \left(\frac{v}{v_d}\right)^2\right] \frac{\partial^2 \overline{w}_b}{\partial \overline{\eta}^2} \,. \qquad (8)$$

The final result for this model is the following differential equation

$$A_4 \frac{\partial^4 \overline{w}_b}{\partial \overline{\eta}^4} + A_2 \frac{\partial^2 \overline{w}_b}{\partial \overline{\eta}^2} + A_0 \overline{w}_b = F\left(\overline{\eta}\right) \,, \qquad (9)$$

15

where the coefficients are given by

$$
\begin{aligned}
A_4 &= \left[\left(\frac{v}{v_d}\right)^2 - 1\right]\left[\left(\frac{v}{v_s}\right)^2 - 1\right] , \\
A_2 &= \left(\frac{v}{v_d}\right)^2\left[1 + \beta^2\left(\frac{v_d}{v_s}\right)^2\right] - \beta^2\left(1 - \nu^2\right)\left(\frac{v_d}{v_s}\right)^2 , \\
A_0 &= \beta^2 + \frac{\beta^2\nu^2}{\left[\left(\frac{v}{v_d}\right)^2 - 1\right]} , \\
F(\overline{\eta}) &= \beta^2\left(1 - \nu^2\right)\left\{\Lambda_1 + (\Lambda_3 - \Lambda_1)\left[1 - H(\overline{\eta})\right]\right\} \\
&\quad + \beta^2\left(1 - \nu^2\right)\left\{(\Lambda_2 - \Lambda_3)\left[1 - H(\overline{\eta})\right]e^{\frac{\overline{\eta}}{\eta_0}}\right\} .
\end{aligned}
\tag{10}
$$

In these expressions, $H(\overline{\eta})$ is the step function and $\eta_0 = \dfrac{\sqrt{12}vT}{h}$.

2.2 DISPERSION EQUATION

The solution of the differential equation (9) consists of a homogeneous and an inhomogeneous part. By assuming an exponential dependence of the form $\overline{w}_b \sim exp(\alpha\overline{\eta})$ for the homogeneous part, the following dispersion equation is obtained

$$
A_4\,\alpha^4 + A_2\,\alpha^2 + A_0 = 0 ,
\tag{11}
$$

where the quantity α is related to the wave number k through

$$
k = \frac{\sqrt{12}\alpha}{ih} .
\tag{12}
$$

16

The characteristic roots can be determined for each value of v by simply using the quadratic formula. Based on the values of the speed v, five different cases can be distinguished. In the present investigation, only the first two are relevant. In the first case, $0 < v < v_{c0}$, the values of α are complex: $\alpha = \pm n \pm im$. In the second case, $v_{c0} < v < v_{c1}$, the values of α are purely imaginary: $\alpha = \pm im_1$ and $\alpha = \pm im_2$, where $m_1 < m_2$. The speed v_{c0} is the first critical velocity. The value of the critical velocity v_{c0} can be calculated from the vanishing of the discriminant

$$A_2^2 - 4A_0 A_4 = 0 \ . \tag{13}$$

For the Tang model, there are four critical velocities. The other critical velocities are v_{c1}: the shear wave speed v_s, v_{c2}: the dilatational wave speed in a bar $v_d \sqrt{1 - \nu^2}$, and v_{c3}: the dilatational wave speed v_d. For a more detailed discussion on these five cases, the reader is referred to Tang [13].

2.3 CASE 1: $0 < v < v_{c0}$

Case 1 is referred to as the subcritical case. The axial direction is split up into two regions. Region I is the region after the detonation, $\overline{\eta} < 0$, and region II is the region ahead of the detonation, $\overline{\eta} \geq 0$. For subcritical velocities, there are four complex roots. At $\overline{\eta} = 0$, continuity conditions have to be satisfied

17

for displacement, rotation, moment, and shear. Furthermore, the solution must remain bounded for $\overline{\eta} \to \pm\infty$. The final solution is:

$$
\begin{aligned}
\overline{w}_b^I &= \Lambda_1^s + (\Lambda_3^s - \Lambda_1^s) \left\{ 1 + \frac{1}{8} e^{n\overline{\eta}} \left[-4\cos(m\overline{\eta}) + 2\frac{n^2 - m^2}{nm} \sin(m\overline{\eta}) \right] \right\} \\
&\quad + \left(\Lambda_2^d - \Lambda_3^d \right) e^{\frac{\overline{\eta}}{\overline{\eta}_0}} \\
&\quad + \left(\Lambda_2^d - \Lambda_3^d \right) \frac{1}{4} e^{n\overline{\eta}} \\
&\qquad \left\{ \left[-2 + \left(\frac{1}{\overline{\eta}_0} \right) \frac{m^2 - 3n^2}{n(n^2 + m^2)} + \left(\frac{1}{\overline{\eta}_0} \right)^3 \frac{1}{n(n^2 + m^2)} \right] \cos(m\overline{\eta}) \right. \\
&\qquad + \left[\frac{n^2 - m^2}{mn} + \left(\frac{1}{\overline{\eta}_0} \right) \frac{n^2 - 3m^2}{m(n^2 + m^2)} - \left(\frac{1}{\overline{\eta}_0} \right)^2 \frac{1}{mn} \right. \\
&\qquad \left. \left. - \left(\frac{1}{\overline{\eta}_0} \right)^3 \frac{1}{m(n^2 + m^2)} \right] \sin(m\overline{\eta}) \right\} ,
\end{aligned}
\tag{14}
$$

$$
\begin{aligned}
\overline{w}_b^{II} &= \Lambda_1^s + (\Lambda_3^s - \Lambda_1^s) \left\{ \frac{1}{8} e^{-n\overline{\eta}} \left[4\cos(m\overline{\eta}) + 2\frac{n^2 - m^2}{nm} \sin(m\overline{\eta}) \right] \right\} \\
&\quad + \left(\Lambda_2^d - \Lambda_3^d \right) \frac{1}{4} e^{-n\overline{\eta}} \\
&\qquad \left\{ \left[2 + \left(\frac{1}{\overline{\eta}_0} \right) \frac{m^2 - 3n^2}{n(n^2 + m^2)} + \left(\frac{1}{\overline{\eta}_0} \right)^3 \frac{1}{n(n^2 + m^2)} \right] \cos(m\overline{\eta}) \right. \\
&\qquad + \left[\frac{n^2 - m^2}{mn} - \left(\frac{1}{\overline{\eta}_0} \right) \frac{n^2 - 3m^2}{m(n^2 + m^2)} - \left(\frac{1}{\overline{\eta}_0} \right)^2 \frac{1}{mn} \right. \\
&\qquad \left. \left. + \left(\frac{1}{\overline{\eta}_0} \right)^3 \frac{1}{m(n^2 + m^2)} \right] \sin(m\overline{\eta}) \right\} ,
\end{aligned}
\tag{15}
$$

where

$$
\Lambda_j^s = \frac{\beta^2 (1 - \nu^2)}{A_0} \Lambda_j , \qquad \Lambda_j^d = \frac{\beta^2 (1 - \nu^2)}{A_4 \left(\frac{1}{\overline{\eta}_0} \right)^4 + A_2 \left(\frac{1}{\overline{\eta}_0} \right)^2 + A_0} \Lambda_j .
\tag{16}
$$

18

The expressions show that the solution is oscillatory with an exponential decay as the distance increases from the detonation. There are precursor structural waves ahead of the detonation. The frequency of these precursor waves is equal to the frequency of the main signal which exists after the detonation has passed. When the velocity approaches v_{c0}, the value of n goes to zero and the solution becomes unbounded.

2.4 CASE 2: $v_{c0} < v < v_{c1}$

Case 2 is referred to as the supercritical case. For supercritical velocities, there are only purely imaginary roots. The axial direction is again split up into two regions. At $\overline{\eta} = 0$, continuity conditions must be satisfied. For supercritical velocities the solution remains bounded for $\overline{\eta} \to \pm\infty$, so other conditions have to be used to determine the solution. The extra restriction for this case is a radiation condition; energy has to flow away from the pressure step. By using the group velocity concept

$$
\begin{aligned}
\overline{w}_b^I &= \Lambda_1^s + (\Lambda_3^s - \Lambda_1^s)\left\{1 + \left[\frac{m_2^2}{m_1^2 - m_2^2}\right]\cos(m_1\overline{\eta})\right\} \\
&+ \left(\Lambda_2^d - \Lambda_3^d\right)e^{\frac{\overline{\eta}}{\overline{\eta}_0}} \\
&+ \left(\Lambda_2^d - \Lambda_3^d\right)\left[\frac{1}{m_1 m_2 (m_1^2 - m_2^2)}\right]\left\{m_1 m_2\left[m_2^2 + \left(\frac{1}{\overline{\eta}_0}\right)^2\right]\cos(m_1\overline{\eta})\right.
\end{aligned}
\tag{17}
$$

19

$$+ \quad m_2 \left(\frac{1}{\overline{\eta}_0}\right) \left[m_2^2 - \left(\frac{1}{\overline{\eta}_0}\right)^2\right] \sin\left(m_1\overline{\eta}\right) \Bigg\} \ ,$$

$$\overline{w}_b^{II} = \Lambda_1^s + (\Lambda_3^s - \Lambda_1^s) \left[\frac{m_1^2}{m_1^2 - m_2^2}\right] \cos\left(m_2\overline{\eta}\right) \tag{18}$$

$$+ \quad \left(\Lambda_2^d - \Lambda_3^d\right) \left[\frac{1}{m_1 m_2 \left(m_1^2 - m_2^2\right)}\right] \Bigg\{ m_1 m_2 \left[m_2^2 + \left(\frac{1}{\overline{\eta}_0}\right)^2\right] \cos\left(m_2\overline{\eta}\right)$$

$$- \quad m_1 \left(\frac{1}{\overline{\eta}_0}\right) \left[m_1^2 + \left(\frac{1}{\overline{\eta}_0}\right)^2\right] \sin\left(m_2\overline{\eta}\right) \Bigg\} \ .$$

In the supercritical case, the frequencies are different: the precursor wave contains a higher frequency signal than the main wave (see for example Figure 3). As the velocity approaches v_{c0}, m_1 approaches m_2 and the solution becomes unbounded.

3   ANALYTICAL TRANSIENT MODEL

The "steady state" model has severe limitations for making realistic pre-
dictions, particularly near the critical velocity, where the response is pre-
dicted to be infinite. In order to remedy this, the time-dependent equations
of elasticity must be solved. The most quantitative method for doing this is to
use a finite element solution described in Section 4. A less accurate but some-
what simpler method is to consider additional simplifications to the model
and simplify the governing equation so that classical methods of analysis can
be used to construct a time-dependent solution. The simplifications are to
neglect the effects of transverse shear and rotary inertia which is equivalent
to taking $v_s \rightarrow \infty$ and $\left(\frac{v}{v_d} \right) \ll 1$. Starting from this equation, the solution
is obtained as an infinite series of normal modes with time-dependent coef-
ficients computed from the prescribed loading function. In practice, only a
finite number of modes is considered and the time-dependence of the ampli-
tude of each mode can be obtained by analytic solution of a simple ordinary
differential equation. In the following section, the solution for the general
problem is considered and applied to the specific cases of a finite length thin
shell with either simply supported or clamped end conditions.

3.1 BASIC EQUATIONS

Consider a thin shell with length L. As a starting point for the analytical transient model, the original shell equations (3) are simplified by neglecting the terms arising from rotary inertia and transverse shear. The resulting equation is

$$\frac{\partial^4 w}{\partial x^4} + \left(\frac{12}{v_d^2 h^2}\right) \frac{\partial^2 w}{\partial t^2} + \frac{12^2 \beta^2 (1 - \nu^2)}{h^4} w = \frac{12^2}{h^3} F(x,t) \;, \qquad (19)$$

where $F(x,t)$ is the transient loading function. The radial displacement is written as the sum of eigenmodes $\phi_q(x)$

$$w(x,t) = \sum_{q=1}^{\infty} b_q(t)\phi_q(x) \;. \qquad (20)$$

The eigenmodes ϕ_q are obtained by using the method of separation of variables to find the solution to the homogeneous version $(F = 0)$ of equation (19), considering only a single mode, i.e., one term of the series (20).

The resulting equation for the spatial eigenmodes is of the form

$$\frac{\partial^4 \phi_q}{\partial x^4} = \kappa_q \phi_q \;, \qquad (21)$$

where κ_q is the separation constant. The values of κ_q are determined as eigenvalues for equation (21) and will depend on the mode number q, the dimensions, and the boundary conditions for the shell. Solutions for specific

cases are discussed subsequently. For a single mode, the solution for b_q is of the form $b_q \propto \exp(\omega_q t)$. Substituting into the homogeneous version of equation (19), we find that the frequency ω_q and separation constant κ_q are related by

$$\kappa_q = \omega_q^2 \frac{12}{v_d^2 h^2} - \left[\frac{12^2 \beta^2 \left(1 - \nu^2\right)}{h^4} \right] . \tag{22}$$

Once the separation constant κ_q is determined for a specific set of boundary conditions, equation (22) can be used to determine the frequency.

The eigenmodes are orthonormal

$$\int_0^L \phi_q(x)\phi_r(x)dx = \begin{cases} 0 & \text{for } q \neq r \\ \\ 1 & \text{for } q = r \end{cases} . \tag{23}$$

Inserting the modal expansion into the differential equation gives, dropping the (x) notation for ϕ_q and the (t) notation for b_q

$$\sum_{q=1}^{\infty} \left[\left(\frac{12}{v_d^2 h^2} \right) \frac{\partial^2 b_q}{\partial t^2} \phi_q + b_q \left(\frac{\partial^4 \phi_q}{\partial x^4} + \frac{12^2 \beta^2 \left(1 - \nu^2\right)}{h^4} \phi_q \right) \right] = \frac{12^2}{h^3} F(x,t) . \tag{24}$$

Since the functions ϕ_q are eigenmodes, we can use equations (21) and (22) to rewrite this as

$$\sum_{q=1}^{\infty} \left[\frac{\partial^2 b_q}{\partial t^2} \phi_q + \omega_q^2 b_q \phi_q \right] = \frac{12 v_d^2}{h} F(x,t) , \tag{25}$$

where ω_q is the angular eigenfrequency for mode q. Multiplying equation (24)

23

by eigenmode r, integrating with respect to x, and using orthonormality gives

$$\frac{\partial^2 b_q}{\partial t^2} + \omega_q^2 b_q = \frac{12 v_d^2}{h} \int_0^L \phi_q F(x,t) dx \ . \tag{26}$$

The transient loading function for detonation loading can be approximated (see Section 2.1 and Appendix B) as

$$
\begin{aligned}
F(x,t) \ &= \ \beta^2 \left(1 - \nu^2\right) \Lambda_1 \\
&+ \ \beta^2 \left(1 - \nu^2\right) [1 - H(x - vt)] \left\{ (\Lambda_3 - \Lambda_1) + (\Lambda_2 - \Lambda_3) e^{\left[\frac{x-vt}{vT}\right]} \right\} \ .
\end{aligned}
\tag{27}
$$

Substituting this into equation (26), the integral can be carried out once the eigenmodes are given. The result is a second-order ordinary differential equation in time for the coefficients b_q. The approximation to the loading function is valid only for $vt \leq L$, i.e, until the detonation reaches the end of the tube.

$$
\begin{aligned}
\frac{\partial^2 b_q}{\partial t^2} + \omega_q^2 b_q \ &= \ \frac{12 v_d^2 \beta^2 \left(1 - \nu^2\right)}{h} \left\{ \int_0^L \phi_q \left[\Lambda_1\right] dx \right. \\
&+ \left. \int_0^{vt} \phi_q \left[(\Lambda_3 - \Lambda_1) + (\Lambda_2 - \Lambda_3) e^{\left[\frac{x-vt}{vT}\right]} \right] dx \right\} \ .
\end{aligned}
\tag{28}
$$

Eigenfunctions for two cases are described in subsequent sections. In those cases, it is possible to carry out the integration exactly; the results are rather lengthy and are not displayed here. The results for the special case of a simply-supported shell are given in Beltman and Shepherd [15]).

24

The initial conditions for the time integration are

$$b_q(0) = 0 , \qquad \frac{\partial b_q}{\partial t}\bigg|_0 = 0 . \tag{29}$$

3.2 SIMPLY-SUPPORTED SHELL

The eigenmodes and eigenvalues for a simply-supported shell can be obtained by solving equation (21) with the boundary conditions appropriate to a simply-supported elastic structure. For the thin-shell approximation, these correspond to the vanishing of the deflection and the moment at the ends of the tube

$$\phi_q = 0 \qquad \text{and} \qquad \frac{\partial^2 \phi_q}{\partial x^2} = 0 \qquad \text{at} \qquad x = 0 \qquad \text{and} \qquad x = L . \tag{30}$$

The solutions that satisfy these conditions are of the form

$$\phi_q = \sqrt{\frac{2}{L}} \sin\left(\frac{q\pi}{L}x\right) \qquad q = 1, 2 \ldots \infty . \tag{31}$$

This leads to a value of the separation constant

$$\kappa_q = \left(\frac{q\pi}{L}\right)^4 . \tag{32}$$

Substituting into equation (22), the eigenfrequencies for a simply-supported shell are

$$\omega_q^2 = \left(\frac{v_d^2 h^2}{12}\right) \left[\left(\frac{q\pi}{L}\right)^4 + \frac{12^2 \beta^2 \left(1 - \nu^2\right)}{h^4}\right] \qquad q = 1, 2 \ldots \infty . \tag{33}$$

25

3.3 CLAMPED SHELL

The boundary conditions for a clamped shell are

$$\phi_q = 0 \quad\text{and}\quad \frac{\partial \phi_q}{\partial x} = 0 \quad\text{at}\quad x = 0 \quad\text{and}\quad x = L. \qquad (34)$$

The corresponding modes are [1]

$$\phi_q = C_q \left[\cos\left(A_q x\right) - C_1 \sin\left(A_q x\right) - C_2 e^{-A_q(L-x)} - C_3 e^{-A_q x} \right], \qquad (35)$$

where

$$
\begin{aligned}
C_1 &= \frac{\cos(A_q L)e^{-A_q L} - \frac{1}{2}\left(1 + e^{-2A_q L}\right)}{\sin(A_q L)e^{-A_q L} - \frac{1}{2}\left(1 - e^{-2A_q L}\right)} \\
C_2 &= \frac{1}{2}\frac{\sin(A_q L) - \cos(A_q L) + e^{-A_q L}}{\sin(A_q L)e^{-A_q L} - \frac{1}{2}\left(1 - e^{-2A_q L}\right)} \\
C_3 &= \frac{1}{2}\frac{\sin(A_q L)e^{-A_q L} - \cos(A_q L)e^{-A_q L} - 1}{\sin(A_q L)e^{-A_q L} - \frac{1}{2}\left(1 - e^{-2A_q L}\right)}.
\end{aligned}
\qquad (36)
$$

The value of the normalization constant C_q is determined from the orthonormality condition. The eigenvalues A_q are determined from the solution of the transcendental equation

$$\cos\left(A_q L\right)\cosh\left(A_q L\right) = 1, \qquad (37)$$

and the eigenfrequencies are

$$\omega_q^2 = \left(\frac{v_d^2 h^2}{12}\right)\left[A_q^4 + \frac{12^2 \beta^2 \left(1 - \nu^2\right)}{h^4} \right]. \qquad (38)$$

26

4 FINITE ELEMENT SIMULATIONS

The finite element calculations were carried out with the package Ideas [16]. A transient linear elastic calculation was carried out to calculate the structural response to a moving pressure load. For the (middle) tube section, 500 rotatory symmetric solid elements were used in the axial direction and 5 in the radial direction. This model will, therefore, be capable of representing the effects of transverse shear and rotatory inertia and will be more reliable than the transient thin-shell analytical model developed in the previous section. Comparison of the models with each other and the experiment is given in the subsequent sections.

For the strain signals of interest, with a phase speed of approximately 2000 m/s and a frequency of 6 kHz, the finite element computations will have a resolution of about 70 elements per wavelength. This is more than sufficient to accurately resolve the flexural waves. The transient loading is represented by prescribing a force as a function of time at each node. The force history for each node was a discrete version of the exponential approximation to the Taylor-Zeldovich model described in Appendix B. The exponential decay was approximated by 20 linear segments.

In the calculations, a value of $4.34 \cdot 10^{-4}$ s was used for the exponential decay time constant T, which was found in the experiments to be a representative value for the second tube section. For the purposes of computing amplification factors, the response was calculated for the second tube section (see the discussion of the facility in the subsequent section) up to the time that the reflected detonation would enter this tube section again after reflection at the end of the third section. For the time integration, 1000 intervals were used. For the problem of interest, this means approximately 45 steps per oscillation period. The response was calculated with a normal mode superposition technique using 200 modes in the calculations. The modes of vibration of the tube were extracted first. These eigenmodes were then used as a basis to calculate the transient tube response. Calculations were carried out for a clamped tube (see Figure 4) and a simply-supported tube (see Figure 5), where R_{in} is the internal radius of the tube.

5 EXPERIMENTAL SETUP

5.1 THE DETONATION TUBE

A drawing of the GALCIT[2] 280 mm detonation detonation tube is given in Figure 6. The tube consists of three sections that are connected by flanges. Each section is 2.44 m long; the length of tube interior to the flanges is 2.38 m. The internal radius of the tube is 14 cm and the outer radius is 16.5 cm. The tube is made of type 304 stainless steel. Additional details about the facility and the experimental protocol are given in Beltman and Shepherd [15].

Before each experiment, the tube is evacuated. Once the evacuation is completed, the tube is filled to the desired pressure with the mixture of interest. The mixture composition is determined by the method of partial pressures. A bellows pump is used to circulate and mix the components. The detonation is initiated at the left end of the tube by discharging a capacitor (~ 100 J) into a thin wire, vaporizing the wire, and creating a blast wave. Just before the discharge, a small amount of a sensitive acetylene[3]-oxygen driver mixture is injected into the tube near the wire. The detonation of the driver produces a strong blast wave that promptly initiates a detonation

in the main test mixture. When large amounts of diluents are used, the initiation may fail. In case of a misfire, the glow plug is used to burn the mixture. If the initiation is successful, a detonation travels down the tube at an almost constant velocity. Typical velocities range from 1500 m/s to 3000 m/s for most hydrocarbon-oxygen-diluent mixtures. Wave speeds are computed from measured arrival times at piezoelectric transducers located along the tube.

5.2   MATERIAL AND GEOMETRICAL PROPERTIES

The material and geometrical properties of the tube are given in Table 1. The sections are connected by flanges, keys, and bolts. The motion of the tube is restricted by the flanges that press on the keys and the coupler between two tubes. The length of a tube section is the distance between the outer sides of two key grooves. In the finite element calculations, various boundary conditions were imposed at these locations to model the effect of the flanges on flexural wave propagation.

5.3 STRAIN MEASUREMENTS

For the present investigation, 18 strain gages were used (Micro Measurement type WK-13-250BF-10C) to monitor the circumferential strain as a function of time. The locations are given in Table 2 and Figure 7. Note that the distances x_I, x_{II}, and x_{III} are relative to the key.

The strain signals were used as input for balanced Wheatstone bridge circuits. The output voltages were then amplified and fed to the data acquisition system. The sampling rate for the strain and pressure signals was 1 MHz.

5.4 PRESSURE MEASUREMENTS

The pressure was measured at three points. The first and the second transducers were mounted on the second tube section (see Figure 6). The third transducer was mounted on the third tube section. The pressure signals were used only to determine the speed of the detonation. Experimental measurement of the peak value of the pressure is not very reliable but accurate computations can be made of the Chapman Jouguet pressure for a given mixture. Therefore, the amplification factors were all computed using equation (1) and the calculated Chapman-Jouguet pressure for the mixture of interest.

5.5 TEST MIXTURE

The critical velocity of the tube, calculated from the "steady state" analytical model including rotatory inertia and transverse shear, is approximately: $v_{cr} = 1455$ m/s. A stoichiometric hydrogen, H_2, oxygen, O_2, mixture with a variable amount of argon, Ar, as the diluent was used in the experiments:

$$2H_2 + O_2 + N_{Ar}Ar , \tag{39}$$
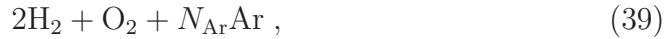
The amount of argon N_{Ar} was used to control the velocity of the detonation over a range of 1300 to 2800 m/s, bracketing the critical velocity. By increasing the amount of diluent, the cell size also increases. The initial pressure of the mixture affects both velocity and cell size. In order to define a series of measurements, the behaviour of the mixture was investigated for a number of conditions. In Figures 8 and 9, the Chapman-Jouguet velocity, pressure, and the detonation cell size are plotted as a function of the amount of diluent. The Chapman-Jouguet velocity and pressure were calculated with the STANJAN program [17]. Measured velocities were typically within 0.5 to 1% of the calculated values. The cell size data were taken from [18, 19, 20, 21, 22, 23, 24].

Figures 8 and 9 show that the Chapman-Jouguet velocity and pressure

decrease, and the cell size increases with increasing amounts of diluent. The detonation velocity is essentially independent of initial pressure variation, as long as the initial pressure is not exceedingly low, whereas the cell size is approximately inversely proportional to the pressure. The Chapman-Jouguet pressure is shown only for one value of the initial pressure (100 kPa) in Figure 8. Values at other initial pressures can be obtained by scaling these values since the Chapman-Jouguet pressure is linearly proportional to the initial pressure at a fixed diluent concentration.

A series of tests was carried out [15] with systematic variation of the mixture parameters. These test series examined separately the effects of detonation velocity, the linearity of the structural response, the effects of flanges and closures, detonation cell size, and repeatability. In the ideal case, the experimental conditions could be chosen in such a way that only one characteristic of the loading profile is changed at a time. Three characteristics were considered: detonation velocity, pressure, and cell width. However, we varied only two parameters, initial pressure and diluent amount, in the mixture that we used. This results in strongly correlated variations in the loading characteristics with changes in say, diluent amount, at fixed initial pressure. Fortunately, in the present experiments, we are primarily dealing

33

with linear (elastic) structural response, and the detonation pressure is not an essential parameter. We have verified this experimentally and have shown [15] that with all other parameters held constant, the structural response can be scaled with the equivalent static response associated with the Chapman-Jouguet pressure. This means that detonation velocity and cell width are the only significant loading characteristics we need to examine.

The linearity of the response was investigated by varying the initial pressure between 25 and 100 kPa for mixtures with modest amounts of dilution. Two detonation velocities, 1800 and 2000 m/s, were examined. The detonation velocities were essentially independent of the initial pressure. For these mixtures, the detonation cell size remains sufficiently small compared to the structural wavelength, so the detonation cellular structure does not play a role in exciting the flexural waves. For the velocity range of interest, the structural wavelength varies between 100 and 300 mm and the cell size is less than 20 mm for these mixtures.

The influence of the detonation velocity was investigated by varying the amount of diluent at a fixed initial pressure of 100 kPa. The range of detonation velocity was between 1400 and 1800 m/s and the detonation cell size was less than 20 mm in all cases. For even higher velocity shots, 1800 to

2800 m/s, a lower initial pressure, 50 kPa, was used to stay within the design limits of the tube. At these high speeds, the amount of diluent is low, $N_{\text{Ar}} \leq 4.3$, and the cell is less than 3 mm. The effect of flanges and closures was examined for the lower velocity range mixtures by placing strain gages close to these features on the tube. The repeatability of the results was examined by carrying out a series of replica tests in the velocity range of 1400 to 1500 m/s.

The influence of the cell size was investigated by varying the initial pressure at high diluent concentrations, $18 \leq N_{\text{Ar}} \leq 25$. The largest cell size in the experiments was 150 mm, of the order of magnitude of the structural wavelength but less than the tube diameter of 280 mm. The pressure and the cell size were simultaneously varied in this case, but the cell size influence can be extracted since the structural response can be scaled with the detonation pressure.

Selected results of these studies are summarized in the next section and more details are provided in [15].

6   RESULTS AND DISCUSSION

6.1   REPRESENTATIVE STRAIN HISTORIES

Representative strain histories for gages 5 and 10 are given in Figures 10 and 11.[4] These results are for detonations in mixtures with an initial pressure of 100 kPa and argon amounts (see Eq 39) of $N_{Ar} = 18.25$ (1400.1 m/s), 14.7 (1478 m/s), 6.85 (1699.7 m/s). Gage 5 is mounted in the first half of the second tube section, 0.79 m from the entrance to that section, and gage 10 is mounted near the end of the second tube section, 2.2 m from the entrance to that section and 0.18 m from the flange between sections two and three. In both figures, the top plot is a strain history for a subcritical velocity, the middle plot is a strain history for a velocity around the critical velocity, and the bottom plot is a supercritical strain history. For detonation speeds of 1400.1 m/s, 1478.8 m/s and 1699.7 m/s, it takes 1.69 ms, 1.61 ms, and 1.40 ms, respectively, to cover this distance. The detonation Chapman-Jouguet pressure is 1.2, 1.35, and 1.7 MPa for these three cases, respectively. On this basis alone, we would expect the peak strains to be higher when the amount of argon dilution is lower. Note that the spike or glitch at about 100 μs is actually due to the electric discharge used to start the detonation.

The strain measured by gage 5 (Figure 10) rapidly increases when the shock wave passes by that location. Following the rapid increase in strain, oscillations with a frequency of about 5 kHz are visible for all three wave velocities. The amplitude of the oscillation is modulated due to the dispersive nature of the waves and at long times, beating between the radial oscillations and flexural waves reflected from the flange between the second and third tube sections. By the time the wave reaches gage 10 (Figure 11) a precursor is visible in front of the main signal. In accordance with the models, the frequency of the precursor is comparable to the main signals for the subcritical and critical cases and higher for the supercritical cases. There is a peak in strain near the time the detonation reaches the gage and the amplitude of the peak strain and the oscillations is highest for the near-critical-speed case. The decay of the oscillations is relatively rapid in all cases. In the supercritical case, the amplitude of the precursor wave is substantially smaller than in the critical or subcritical case.

6.2 COMPARISON WITH MODELS

It is clear just from these selected cases that the strain signals evolve significantly between the location of gage 5 and gage 10. This suggests that

the steady-state model will not be particularly realistic. However, for completeness, we have computed for these cases the hypothetical steady-state response using the Tang model described in Section 2. The results are shown in Figure 12. Since the steady-state model gives results that are independent of gage position, only one trace is shown for each velocity case. The difference between subcritical and supercritical cases is striking with the very high decay rates for all oscillations in the subcritical case and the precursor being completely suppressed in the supercritical case (1699.7 m/s). The precursor extends far ahead of the main signal in the near-critical case, indicating a very small exponential decay rate. Since the steady-state model assumes an infinite length tube, no interference patterns would be expected. The peak amplitudes of the strains are in reasonable agreement with the observation; more detailed results on this aspect are given in subsequent sections.

The transient models give much more realistic results. Computations using the transient analytical model of Section 3 are shown in Figures 13 and 14 for gages 5 and 10. For each gage, results are shown for both the simply supported and clamped boundary conditions. Note that the arrival times on these plots cannot directly be compared with the experimental value because only the second section of the tube has been simulated. The results

are much more realistic than the steady-state model and clearly show that the development of many features in the strain signals are a consequence of unsteady behavior. Both the development of the precursors in gage 10 and the modulation of the oscillations of the main signal are predicted by the transient analytical model. As shown subsequently, the predicted amplitudes of the transient model are also in reasonable agreement with the experimental results if we take into account one crucial factor. The transient analytical model neglects rotatory inertia and shear, which results in the critical velocity being about 100 m/s higher than in the full model or experiments. The clamped and simply-supported results are indistinguishable for gage 5 but there is a clear difference for gage 10, which is close to the flange between the second and third sections. Comparision with the experimental results clearly indicates that the clamped version is much more realistic than the simply-supported.

The most realistic results are given by the FEM model of Section 4. This model can not only correctly calculate the transient development of the strain histories but can also make accurate quantitative predictions since the effects of rotatory inertia and shear are properly included. The strain histories are very similar to those of the analytical transient model and are not shown

here. Detailed comparison with the experiments is given subsequently in the analysis of the amplification factors.

6.3   REFERENCE/REPRODUCIBILITY SHOTS

After each series of shots, a reference shot was conducted in order to verify the system state. In addition, several shots were conducted with the same mixture in order to examine the reproducibility of the test process. The results indicate that the reproducibility for gages 3,5,7,9, and 10 is very good. The maximum difference in peak amplitude for these gages between corresponding shots at approximately the same velocity is less than 2.1%. The reproducibility for gages 4,6, and 8 is not as good and the spread in values is somewhat larger.

6.4 FREQUENCY OF SIGNALS

The analytical steady-state model predicts that a signal has characteristic frequencies that can be obtained from the solutions to the dispersion relation (equation 11). The experimental data for strain gages 3, 5, 7, 9, and 10 were used to extract frequency values and compared to the solution of the dispersion relation. For this purpose, the analytical solution is fit to each strain history, both before and after the detonation had passed. In this way, the frequencies of the precursor wave and the main signal were extracted. The experimental frequency values are compared to theoretical results from the Tang model (see Section 2.2) in Figure 15. For strain gage 3, a curve fit of the precursor signal was not possible due to the weak precursor signal at the entrance of the tube and the corresponding poor signal-to-noise ratio.

The agreement between theory and experiments is reasonable. Two distinct branches are observed above the critical speed. For subcritical velocities, the frequency of the precursor signal and the main signal is approximately the same. In the supercritical case, the high–frequency signal (the upper branch of the curve) is contained in the precursor wave, whereas the low–frequency signal (the lower branch of the curve) is contained in the main signal. The signal-to-noise ratio is low for subcritical cases; this leads to the

apparent existence of a precursor for speeds well below the critical value.

The results clearly demonstrate the transient nature of the process: the frequency content develops as a function of distance. For strain gage 3, the frequency of the main signal is independent of the velocity. This strain gage is located close to the flange at the beginning of the second tube section. The frequency of the signal is close to 5.1 kHz, the frequency of vibration for radial "breathing motion" of a simple cross-sectional model. As the distance from the flange at the beginning of section 2 increases, the flexural waves develop and the strain histories and the corresponding frequencies approach the analytically predicted values.

The wavenumber, k, and the wavelength, λ, can be calculated from the frequency, f, and the speed, v, according to

$$k = \frac{2\pi f}{v} , \qquad \lambda = \frac{v}{f} . \tag{40}$$

For the signals presented in Figure 15, the wavelength of the main signal varies between 0.22 m and 0.34 m. The wavelength of the precursor varies between 0.10 m and 0.22 m.

6.5 AMPLIFICATION FACTORS

One key result of our investigation is the measurement of amplification factors, defined by equation 1 as the ratio of measured peak strain to computed static strain based on the Chapman-Jouguet pressure. The amplification factor is a convenient way to represent the peak loads that can be expected and can be used by designers to incorporate the appropriate safety factors into the specification of piping systems that will be subjected to detonations.

The most important factor in determining the amplification factor is the detonation wave speed. A series of tests was carried out for wave speeds between 1300 and 2800 m/s and the amplification factors were computed for eight gages. The results and comparisons with the models are shown in Figures 16 and 17 for gages 3-10. To avoid cluttering up the plots, we have made two separate sets of comparisons with the different models. In Figure 16, the experimental results are compared with the results from the analytical "steady-state" model and the finite element results. In Figure 17, the experimental results are compared with the results from the analytical "steady-state" model and the analytical transient models. In the analytical transient model, only the first 300 modes were used.

The results show the dramatic increase of the amplification factor near

the critical velocity once the strain oscillations have developed, i.e., after gage location 5. The experimental results indicate that the critical velocity of the tube is about 1450 m/s. This is very close to the value that was predicted with the analytical "steady-state" model: 1455 m/s. The critical speed calculated with the transient thin-shell models is higher, 1543 m/s, due to the fact that in the transient models the effects of rotatory inertia and transverse shear are neglected. The critical velocity extracted from the finite element results is about 1500 m/s. In general, the finite element model appears to give the best overall agreement with the experimental measurements.

The amplification factors predicted by the steady-state model are obviously not realistic close to the critical speed since a linear model with no damping will always predict an infinite response at the resonant frequency. However, sufficiently far from the resonance, the steady-state model correctly predicts that the amplification factor approaches one for very subcritical waves and is bounded by two for supercritical waves. A maximum amplification factor of two is often used for shock or detonation loading. The present results show that near the critical speed, amplification factors larger than three are possible and in some cases (see the subsequent sections) may be as high as four. The dependence of the amplification factor on the wave speed

and profile is discussed in more detail in the subsequent section.

The growth of the amplification factor with distance from the flange is clearly shown in both the experimental data and predicted by the transient models. The finite element model for the clamped tube is also able to predict the amplification caused by the reflection and interference of waves. Note that the analytical "steady state" model gives the same amplification curve for each strain gage since it assumes a "steady state" situation for a tube of infinite length. Due to the use of the simplified thin-shell theory, the amplifications from the transient analytical models are too high and the peaks are displaced from the correct velocities. However, for design purposes, these models are very useful to obtain a good first estimate. Finite element models can then be used for a more detailed analysis.

The finite element results and the analytical transient model for several strain gages both have resonance-like features, "bumps" in the amplification curves, that are not observed in the experimental data. Examples include two small peaks in the model solutions near the critical velocity in Figure 16a and Figure 17a; broad peaks between the critial velocity and 2000 m/s in Figure 16f, g, and h, and also, Figures 17f, g, and h. We believe that these features are due to wave reflections at the joints in the models and do not

appear in the experimental data because of the nature of the connections between the flanges. These connections are complex and not well enough understood to model without a significant research effort that goes well beyond the scope of the present work. Apparently, there is sufficient damping created by nonuniform contact, friction, and the elastomer seals such that flexural waves are primarily absorbed and dissipated in the joints rather than reflected or transmitted. On the other hand, there is no damping in either the transient analytical model or the finite element model, leading to wave reflections and interactions that cause large amplifications at particular wave speeds where constructive interference is favored. This conclusion is based on detailed examination of the spatial and temporal dependence of the flexural waves in individual simulations.

6.6 INFLUENCE OF PRESSURE LOADING PARAM-ETERS

The pressure profile used to model the detonation loading on the tube contains several parameters, p_1, p_2, p_3, and T. The pressure parameters p_i determine the maximum extent of the deformation in a simple fashion since the elastic motions are linearly proportional to the applied pressure, all other factors being equal. The exponential decay constant T enters in a less obvious fashion. As discussed in Appendix B, the decay time, T, linearly increases as the detonation travels down the tube. For the present study, the decay time for the second tube section varies between 0.4 and 1.2 ms but, for simplicity, we chose this to be a constant, equal to 0.43 ms.

In order to apply the present results to other situations with very short or very long tubes, it is necessary to consider how varying the time constant affects the amplification factors. To do this, amplification curves were calculated with the "steady-state" analytical model for different values of the nondimensional decay time $\eta_0 = \sqrt{12}vT/h$ (see Section 2.1). The results are given in Figure 18. In the calculations, the peak pressure p_2 is equal to the Chapman-Jouguet pressure p_{cj}, and the final pressure p_3 is equal to 0.4 p_2

(see Appendix B).

Evidently, for $\eta_0 \to \infty$, the solution converges to the solution for shock loading between p_1 and p_2. For $\eta_0 \to 0$, the solution for shock loading between p_1 and p_3 is obtained. Thus, the upper bound of the amplification curve is given by shock loading between p_1 and p_2. The lower bound of the amplification curve is given by shock loading between p_1 and $p_3 = 0.4\ p_2$. Depending on the value of T, an amplification curve is obtained somewhere in between these curves. For the second tube section, the decay factor η_0 varies between 130 and 200. Figure 18 suggests that for these decay factors, the response is very close to the result for shock loading between p_1 and p_2.

The dependence of amplification factor on detonation speed is similar for all values of η_0. The peak in the response curves of Figure 18 are associated with the critical velocity and appear in the same location (detonation speed) for all values of η_0. What is also of interest are the values for the amplification factor reached in the limit of very small or very large shock speed. Consider for the moment, the case of large η_0, corresponding to a large decay time. For small values of the velocity, the amplification factor tends to 1. This corresponds to the case of static loading of a single degree of freedom structure; in the present case, the degree of freedom is the radial motion.

This can be verified directly by taking the limit $v \to 0$ in the solution for the steady-state analytical model. For large values of the velocity, but still small compared to the shear wave speed, the amplification factor appears to tend toward a limiting value of two. It is more difficult to extract an analytical bound from a limiting process on the steady-state analytical model, but judging from Figure 18, a value of 2 appears to be appropriate. This is also in agreement with the maximum value that can be obtained from the "sudden" loading of a single degree of freedom system.

6.7   FLANGES AND END EFFECTS

Our preliminary studies indicated that wave interference effects play a significant role in creating high peak strains near the flanges. These effects were investigated in a series of tests in which strain gages were placed very close to the flanges, on the flange itself, and close to the end of the tube (see Figure 7). Amplification factors were measured for gages 11, 12, 13, 15, 16, 17, and 18 for wave velocities between 1300 and 1700 m/s. The results are given in Figure 19.

Due to the reflection and interference of waves, the amplification for gage 11 is high but smaller than the amplification for gage 10. This is probably due to the stiffening effect of the nearby flange. The amplification for gage 12 on the coupler between the flange indicates that the deflection is much smaller on this component than on the main tube. The connection between the tube and the flange only transmits a part of the wave to the coupler, even near the critical velocity. The amplification curve for gage 13, mounted just after the flanges, shows no amplification effect. For the entire velocity range, the amplification is essentially equal to one. This implies that the build-up of the profile starts all over again following a joint between the tube sections. Thus, the flanges and keys prevent transmission of structural waves between

the tube sections but they introduce reflection and interference of waves.

The strains near the far end of the tube are relatively large, see Figure 19 gages 15, 16, 17, and 18. At the far end of the tube, the detonation reflects from the closed end. This results in the peak pressure increasing by up to 2.5 times the Chapman-Jouguet pressure p_2. This pressure increase combined with wave reflection and interaction causes the amplification factor to be almost four (gage 17) on the portion of the tube closest to the end flange.

6.8 LINEARITY AND COMPARISON OF SECTIONS

The linearity of the structural response with the applied load was tested by varying the load pressure p_2 at a fixed detonation velocity. The load (Chapman-Jouguet) pressure was varied over a factor of four by varying the initial pressure between 25 and 100 kPa while simultaneously varying the argon amount N_{Ar} so that the velocity remained fixed. Two velocities were investigated, 1800 and 2000 m/s. The cell width is relatively small for these mixtures, less than 20 mm, in comparison to the structural oscillation wavelengths of 100 to 300 mm, and the cellular structure of the detonation will not be a factor in these tests. Tests designed to specifically examine the effect of cellular structure are discussed in the next section.

The amplification factor versus the Chapman-Jouguet pressure is given in Table 3 for a velocity of 1800 m/s and in Table 4 for a velocity of 2000 m/s. The results show that the amplification factor is nearly independent of the load pressure, supporting the use of linear theory.

In addition, sets of gages at corresponding locations within each of the tube sections give similar amplification factors. Gages 1, 6, and 14 are all located 1.18 m from the start of each section. Gages 2, 8, and 15 are all located 1.95 m from the start of each section. The amplification factors vary at most by 10% for each of these sets of gages, except for gage 15. This gage shows a significantly higher amplification level due to the reflected wave from the closed end of the tube. The comparable values for the amplification factor at equivalent gage locations in the different sections provide further support for the conclusion that the tube can be regarded as a series of independent sections. The amplification values for supercritical speeds are, in all cases, (except gage 15) bounded by two as predicted by simple cross–sectional models.

6.9 CELL SIZE

The cellular structure of the detonation creates an oscillation in the pressure loading (see Figure 20). The oscillations are clearly visible in the pressure signal from pressure gage 3 located in the last section in the tube. This raises the possibility of resonant excitation of flexural oscillations by the pressure oscillations in the detonation. We have examined the effect of detonation cellular structure in a series of tests in which the initial pressure and diluent amount was varied to give cell widths varying between 15 and 150 mm. The diluent amount was adjusted slightly in order to keep the detonation velocity constant within $\pm$ 10 m/s. All other factors being the same, the cell size is approximately inversely proportional to the initial pressure for the mixtures of interest.

The amplification factor as a function of the cell width is given in Figure 21 for a detonation velocity of 1400 m/s. Since linearity was demonstrated in Section 6.8, the increase in amplification with increasing cell width can be attributed to cell size effects. As the cell size becomes comparable to the flexural oscillation wavelength, the flexural waves in the tube are preferentially excited. This can be seen from the increase in the amplification factor with increasing cell width for all gage stations. The effect is fairly dramatic

for these mixtures since the detonation velocity is only 50 m/s lower than the critical velocity.

The effect is less dramatic but still observable for lower velocity detonations. The amplification factor as a function of the Chapman-Jouguet pressure is given in Figure 22 for a velocity of 1267.4 m/s. For gages 3, 4, 5, and 6, there is a clear increase in amplification factor with increasing cell width. However, for gages 7, 8, 9, and 10, there appears to be no dependence on cell width. Due to the inherently unsteady nature of the detonation cellular instability, the loading has now become a function of distance. The loading for these cases deviates from the assumed exponential decay profile. Figure 20 shows pressure signals from a 1267 m/s detonation with a cell width of 150 mm. Clearly the profile is developing with distance and very different from the ideal case in the latter portion of the tube. This change in the pressure history with distance apparently results in much more complex transient coupling phenomena between the pressure loading and flexural waves.

7 CONCLUSIONS

Experiments and analyses indicate that flexural waves and the critical velocity concept are very important when designing tubes that will be subjected to detonation loads. This has been demonstrated by carrying out an extensive series of experiments and modeling with both analytical and numerical simulations. We find that for detonations traveling near the critical speeds it is possible to have deflections that are as high as 3.5 times the static deflection corresponding to the peak pressure in the detonation.

Simple analytical models can be used to predict the critical velocity. Experiments indicate that the critical velocity for the GALCIT detonation tube is approximately 1450 m/s. The "steady-state" analytical model based on a thick-wall formulation including shear and rotary inertia predicts a value of 1455 m/s while the more simplified thin-wall model gives a value of 1543 m/s. A transient finite-element model gave a value of approximately 1500 m/s.

We have compared the measured and simulated strain signals for detonations with velocities between 1400 and 2900 m/s. We separately investigated the effects of detonation cell width and detonation velocity by varying both the amount of dilution and the initial pressure of hydrogen-oxygen-argon

mixtures. Repeat experiments demonstrated that the peak value of the measured strain was reproducible within 2 to 4%. The linearity of the response was examined by carrying out tests at different initial pressures. In the range we studied, the response was linear and the detonation cell width did not have an effect until it became comparable to the wave length of the flexural wave. When the cell size and the structural wave length are of the same order of magnitude, the flexural waves are excited particularly well. This leads to the highest amplification factor measured in the present study: 3.9.

The finite element simulations were used to predict the transient development of the deflection profile and the variation of the amplification factor with detonation velocity. The calculations for a clamped tube show reasonable agreement with the experimental results. Predicted and measured amplification factors are in reasonable agreement except for features associated with wave reflections which cannot be reproduced since the boundary conditions associated with the flanged connections could not be properly simulated with our simplified models. The qualitative features (precursor waves, modulation of the waveform) were reproduced and a frequency analysis of the experimental signals was in good quantitative agreement with the thick-walled tube model.

The experimental results indicate that the flanged connections between tube sections effectively prevent transmission of the structural waves to the next tube section. Since the waves are reflected at the flanges, interference between forward travelling and reflected waves leads to high strains in locations just ahead of the flanges. Following a flanged connection, the flexural wave amplitude was small and increased with increasing distance from the flange. For subcritical waves, the amplification factor reaches an asymptotic value, typically slightly less than one, at large distances from the flange. For supercritical waves, the amplification factor reaches an asymptotic value of slightly less than two at large distances from the flange. The thin-wall, steady-state analytical model was used to estimate the value of the asymptotic amplification for sub- and super-critical waves and this is found to depend strongly on the decay rate of the wave. The faster the decay rate, the smaller the value of the asymptotic amplification factor. For the cases we investigated, the decay time was sufficiently long that the loading was comparable to that of a shock wave with a pressure equal to the Chapman-Jouguet pressure. For near-critical waves, the amplitude is observed to continue to increase with increasing distance rather than saturate. Due to the modest length of our tube sections and interference effects from the flanges, the growth rate

57

could not be determined experimentally. Computations with the thin-tube model confirmed that the peak amplitude of the flexural wave increases with increasing distance for near-critical speed detonation waves.

ACKNOWLEDGMENTS

References

[1] W.M. Beltman, E.N. Burcsu, J.E. Shepherd, and L. Zuhal 1999 *Journal of Pressure Vessel Technology* 121, 315–322. The structural response of tubes to internal shock loading.

[2] W. Fickett and W.C. Davis 1979 *Detonation.* University of California Press Berkeley, CA.

[3] G.I. Taylor 1950 *Proc. Roy. Soc. London* A200, 235–247. The dynamics of combustion fronts behind plane and spherical detonations.

[4] Ya. B. Zeldovich 1942 *Journal Experimental Theoretical Physics* 12(1), 389. On the distribution of pressure and velocity in the products of a detonation explosion, specifically in the case of spherical propagation of the detonation wave.

[5] M.C. de Malherbe, R.D. Wing, A.J. Laderman, and A.K. Oppenheim 1966 *Journal of Mechanical Engineering Science* 8(1), 91–98. Response of a cylindrical shell to internal blast loading.

[6] J.E. Shepherd September 1992 Technical Report A-3991 Brookhaven National Laboratory. Upton, New York 11973. Pressure loads and

structural response on the BNL high-temperature detonation tube.

[7] A. van de Ven, H. Olivier, and H. Grönig. In *7th International Colloquium on Dust Explosions* Bergen 1996. Dynamic structural response of a dust detonation tube.

[8] A. Sperber, H.P. Schildber, and S. Schlehlein 1999 *Shock and Vibration* 6, 29–43. Dynamic load on a pipe caused by acetylene detonations - experiments and theoretical approaches.

[9] T.E. Simkins July 1987 Technical Report ARCCB–TR–87008 US Army Armament Research, Development and Engineering Center. Watervliet, N.Y. 12189–4050. Resonance of flexural waves in gun tubes.

[10] T.E. Simkins, G.A. Pflegl, and E.G. Stilson 1993 *Journal of Sound and Vibration* 168(3), 549–557. Dynamic strains in a 60mm gun tube - an experimental-study.

[11] T.E. Simkins 1994 *Journal of Sound and Vibration* 172(2), 145–154. Amplification of flexural waves in gun tubes.

[12] T.E. Simkins 1995 *Journal of Applied Mechanics-Transactions of the ASME* 62(1), 262–265. The influence of transient flexural waves on dynamic strains in cylinders.

[13] S. Tang. In *Proceedings of the American Society of Civil Engineers* volume 5 , 97–122. Engineering Mechanics Division October 1965 Dynamic response of a tube under moving pressure.

[14] H. Reismann. In S. Ostrach and R.H. Scanlon, editors, *Eighth Midwest Mechanics Conference* , 349–363. Pergamon Press 1965 Response of a pre-stressed cylindrical shell to moving pressure load.

[15] W.M. Beltman and J.E. Shepherd April 1998 Technical Report FM98-3 California Institute of Technology. Pasadena, CA 91125. The structural response of tubes to detonation and shock loading. Parts I and II.

[16] SDRC Technical report SDRC. I-DEAS manual.

[17] W.C. Reynolds 1986 Technical report Mechanical Engineering Department, Stanford University. The element potential method for chemical equilibrium analysis: implementation in the interactive program STANJAN.

[18] T.J. Anderson and E.K. Dabora 1992 *24th Symp. Int. Combust. Proc.* , 1853–1860. Measurements of normal detonation wave structure using Rayleigh imaging.

[19] H.O. Barthel 1974 *Phys. Fluids* 17(8), 1547–1553. Predicted spacings in hydrogen-oxygen-argon detonations.

[20] R.K. Kumar 1990 *Combust. Flame* 80(2), 157–169. Detonation cell widths in hydrogen-oxygen-diluent mixtures.

[21] J.H Lee and H. Matsui 1977 *Combust. Flame* 28(1), 61–66. A comparison of the critical energies for direct initiation of spherical detonation in acetylene-oxygen mixtures.

[22] R.A. Strehlow 1969 *AIAA Journal* 7(3), 492–496. Transverse waves in detonations: II. Structure and spacing in H_2-O_2, C_2H_2-O_2, C_2H_4-O_2 and CH_4-O_2 systems.

[23] R.A. Strehlow, R. Liangminas, R.H. Watson, and J.R. Eyman 1967 *11th Symp. Int. Combust. Proc.* , 683–692. Transverse wave structure in detonations.

[24] R.A. Strehlow, R.E. Maurer, , and S. Rajan 1969 *AIAA Journal* 2(7), 323–328. Transverse waves in detonations: I. Spacings in the hydrogen-oxygen system.

APPENDIX A: NOMENCLATURE

A	eigenvalue	$1/\mathrm{m}$
A_4	dispersion premultiplication factor	
A_2	dispersion premultiplication factor	
A_0	dispersion premultiplication factor	
C	constant	$1/\sqrt{\mathrm{m}}$
C_1, C_2, C_3	constants	
E	Young's modulus	$\mathrm{N/m^2}$
F	dimensionless loading function	
G	shear modulus	$\mathrm{N/m^2}$
H	step function	
H_2	hydrogen	
L	length of shell	m
M_{xx}	moment resultant	N
N_{Ar}	amount of argon	
N_{xx}	axial stress resultant	$\mathrm{N/m}$
$N_{\theta\theta}$	circumferential stress resultant	$\mathrm{N/m}$
O_2	oxygen	
Q_x	shear stress resultant	$\mathrm{N/m}$

R	mean radius	m
R_{in}	inner radius of tube	m
R_{out}	outer radius of tube	m
T	exponential decay factor	s
a	constant of proportionality in decay factor	
b_q	participation factor	$\text{m}\sqrt{\text{m}}$
f	frequency	Hz
h	shell thickness	m
i	imaginary unit	
k	wave number	1/m
m, m_1, m_2	characteristic roots	
n, n_1, n_2	characteristic roots	
p_{cj}	Chapman-Jouguet detonation pressure	Pa
p_1	pre-detonation pressure	Pa
p_2	peak-detonation pressure	Pa
p_{atm}	atmospheric pressure	Pa
p_3	final pressure	Pa
t	time	s

u	axial deflection	m
$\overline{u}$	dimensionless axial deflection	
v	load speed	m/s
v_{cj}	Chapman-Jouguet detonation speed	m/s
v_{c0}	critical velocity	m/s
$v_{c1} = v_s$	shear wave velocity	m/s
$v_{c2} = v_d\sqrt{1 - \nu^2}$	dilatational wave velocity in a bar	m/s
$v_{c3} = v_d$	dilatational wave velocity	m/s
v_d	dilatational wave speed	m/s
v_s	shear wave speed	m/s
w	radial deflection	m
$\overline{w} = \overline{w}_b + \overline{w}_s$	dimensionless radial deflection	
$\overline{w}_b^I$	dimensionless radial deflection $\overline{w}_b$ in region I	
$\overline{w}_b^{II}$	dimensionless radial deflection $\overline{w}_b$ in region II	
x	axial coordinate	m
x_I	axial coordinate tube section I	m
x_{II}	axial coordinate tube section II	m
x_{III}	axial coordinate tube section III	m

α	characteristic root	
β	shell thickness parameter	
$\overline{\eta}$	dimensionless (moving) axial coordinate	
$\overline{\eta}_0$	dimensionless exponential decay factor	
Δp	pressure difference across shell	Pa
κ	shear correction factor	
κ_q	separation constant	
ν	Poisson's ratio	
ρ	density	kg/m^3
ψ	rotation	
$\overline{\psi}$	rotation	
λ	wavelength	m
Λ_j	excitation parameter $(j = 1, 2, \infty)$	
Λ_j^d	excitation parameter $(j = 1, 2, \infty)$	
Λ_j^s	excitation parameter $(j = 1, 2, \infty)$	
ϕ_q	mode shape q	$1/\sqrt{\text{m}}$
ω_q	angular frequency of mode q	1/s

APPENDIX B: PRESSURE

DISTRIBUTION

The Chapman-Jouguet model of an ideal detonation can be combined with the Taylor-Zeldovich similarity solution to obtain an analytic solution to the flow field behind a steadily-propagating detonation in a tube. This solution can be constructed piecewise by considering the three regions shown on Figure 1: the stationary reactants ahead of the detonation mixture, the expansion wave behind the detonation, and the stationary products next to the closed end of the tube.

In this model, the detonation travels down the tube at a constant speed v equal to the Chapman-Jouguet velocity v_{cj}. The corresponding peak pressure, p_2, is the Chapman-Jouguet pressure p_{cj}. The Von Neumann pressure spike is neglected in the present study. The sound speed distribution within the expansion wave can be calculated with the method of characteristics [3, 4] and is

$$\frac{c}{c_3} = \frac{2}{\gamma+1} + \frac{\gamma-1}{\gamma+1}\frac{x}{c_3 t} = 1 - \frac{\gamma-1}{\gamma+1}\left(1 - \frac{x}{c_3 t}\right) , \qquad \text{(B.1)}$$

where c_3 is calculated from

$$c_3 = \frac{\gamma+1}{2}c_{cj} - \frac{\gamma-1}{2}v_{cj} . \qquad \text{(B.2)}$$

68

Expression (B.1) is valid in the expansion wave, *i.e.* for $c_3 t \leq x \leq v_{cj} t$. The values of the ratio of specific heats, γ, and the isentropic sound speed, c_{cj}, are determined with the STANJAN program [17] and depend on the chemical composition of the mixture and the initial thermodynamic state. The other properties are found from the following isentropic relations

$$\frac{c}{c_3} = \left(\frac{T}{T_3}\right)^{\frac{1}{2}} \quad ; \quad \frac{p}{p_3} = \left(\frac{\rho}{\rho_3}\right)^{\gamma} \quad ; \quad \frac{T}{T_3} = \left(\frac{\rho}{\rho_3}\right)^{\gamma-1} \tag{B.3}$$

where T is the temperature, ρ is the density, and p is the pressure. The subscript 3 refers to the conditions at the end of the expansion wave. The pressure p_3 is calculated from

$$p_3 = p_{cj} \left(\frac{c_3}{c_{cj}}\right)^{\frac{2\gamma}{\gamma-1}} \quad . \tag{B.4}$$

This finally gives for the pressure in the expansion wave

$$p = p_3 \left(1 - \left(\frac{\gamma-1}{\gamma+1}\right)\left[1 - \frac{x}{c_3 t}\right]\right)^{\frac{2\gamma}{\gamma-1}} \quad . \tag{B.5}$$

The complete expression for the pressure in the wave is

$$p(x,t) = \begin{cases} p_1 & v_{CJ} < x/t < \infty \\ p_3 \left(1 - \left(\frac{\gamma-1}{\gamma+1}\right)\left[1 - \frac{x}{c_3 t}\right]\right)^{\frac{2\gamma}{\gamma-1}} & c_3 < x/t < v_{CJ} \\ p_3 & 0 < x/t < c_3 \end{cases} \tag{B.6}$$

The expression (B.6) can be used to exactly determine the pressure distribution in the expansion wave. However, this is rather complex for the

purposes of computing the integrals needed for the FEM modeling and the pressure history for a given point can be approximated with an exponential decay function. At a fixed point in space, the variation of pressure with time can be represented by

$$p(x,t) = \begin{cases} p_1 & 0 < t < t_{cj} \\ (p_2 - p_3)\exp\left(-(t - t_{cj})/T\right) + p_3 & t_{cj} < t < \infty \end{cases} \tag{B.7}$$

where $t_{cj} = x/v_{cj}$ is the time it takes for a detonation to travel from the origin to the measurement location x. The time constant T can be determined by fitting the exponential relationship to the exact expression or experimental data. The peak pressure, $p_2 = p_{cj}$, and the final pressure in the expansion wave, p_3, are determined from the CJ-TZ model. The decay time T was determined by fitting the exact solution (B.6) for a range of values of γ.

By inspection of the argument in the exact expression, we see that the time constant T should have the form

$$T = at_{cj} = a\frac{x}{v_{cj}} \; . \tag{B.8}$$

The constant a is a function of the ratio of specific heats γ and the parameter v_{cj}/c_3. Computations of these parameters show that $1.9 < v_{cj}/c_3 < 2$ for a wide range of values of γ and detonation Mach numbers $5 < M_{cj} < 10$. Fitting

the exponential function to the pressure variation in the expansion wave for this range of parameters yields $0.31 < a < 0.34$. A useful approximation is

$$T \approx \frac{t_{cj}}{3} \; . \tag{B.9}$$

In actual practice, if we are trying to represent the variation of pressure over a limited portion of a detonation tube, it is sufficient to take T to be a constant and this can be evaluated at some intermediate location within the portion of the tube that is of interest. This is the procedure used in our study. Figure B.1 shows an example of the exact pressure trace and the approximated exponential decay.

List of figure captions

Figure 1: Detonation propagation in tube with a closed end.

Figure 2: Pressure versus time for detonation loading a) measured, b) ideal model.

Figure 3: Example of circumferential strain versus time for detonation loading. Gage 10, $N_{Ar} = 6.85$, 100 kPa initial pressure. The interference patterns are due to the reflected waves associated with the clamp at nearby end of the tube segment.

Figure 4: Finite element mesh for the clamped tube section. In the actual computation, there are 500 elements in the axial direction and 5 in the radial direction.

Figure 5: Finite element mesh for the simply-supported tube section. In the actual computation, there are 500 elements in the axial direction and 5 in the radial direction.

Figure 6: The GALCIT 280 mm detonation tube facility; see Table 1 for dimensions.

Figure 7: Locations of strain gages; see Table 2 for actual numerical values of axial positions.

Figure 8: Properties of the test mixture: (a) computed CJ detonation speed. ——: initial pressure 25 kP, ——: 50 kPa, − −: 100 kPa; (b) computed CJ detonation pressure for 100 kPa initial pressure.

Figure 9: Properties of the test mixture: detonation cell size. ⋄: initial pressure 25 kPa, +: 50 kPa, □: 105 kPa.

Figure 10: Measured strain signals for strain gage 5. (a) Detonation velocity of 1400.1 m/s. (b) Detonation velocity of 1478.8 m/s. (c) Detonation velocity of 1699.7 m/s.

Figure 11: Measured strain signals for strain gage 10. (a) Detonation velocity of 1400.1 m/s. (b) Detonation velocity of 1478.8 m/s. (c) Detonation velocity of 1699.7 m/s.

Figure 12: Steady-state analytical model strain predictions for the cases shown in Figures 10 and 11. The arrival time of the detonation wave is offset because only the second section of the tube is simulated. (a) Detonation velocity of 1400.1 m/s. (b) Detonation velocity of 1478.8 m/s. (c) Detonation velocity of 1699.7 m/s.

Figure 13: Analytical transient model strain predictions for gage 5 corresponding to the conditions in Figure 10. Left column is for simply-supported end conditions, the right column is for clamped end conditions. (a) and (b), Detonation velocity of 1400.1 m/s. (c) and (d) Detonation velocity of 1478.8 m/s. (e) and (f) Detonation velocity of 1699.7 m/s.

Figure 14: Analytical transient model strain predictions for gage 10 corresponding to the conditions in Figure 11. Left column is for simply-supported end conditions, the right column is for clamped end conditions. (a) and (b),

Detonation velocity of 1400.1 m/s. (c) and (d) Detonation velocity of 1478.8 m/s. (e) and (f) Detonation velocity of 1699.7 m/s.

Figure 15: Characteristic frequencies of strain gage signals: — Tang model, ◇ experiments. (a) Gage 3. (b) Gage 5. (c) Gage 7. (d) Gage 9. (e) Gage 10.

Figure 16: Amplification factor for entire range of detonation velocities. —: FEM clamped, — —: FEM simply-supported, −−: Tang model, ◇: experiments (a) Gage 3. (b) Gage 4. (c) Gage 5. (d) Gage 6. (e) Gage 7. (f) Gage 8. (g) Gage 9. (h) Gage 10.

Figure 17: Amplification factor for entire range of detonation velocities. —: analytical transient clamped, — —: analytical transient simply-supported, −−: Tang model, ◇: experiments (a) Gage 3. (b) Gage 4. (c) Gage 5. (d) Gage 6. (e) Gage 7. (f) Gage 8. (g) Gage 9. (h) Gage 10.

Figure 18: Amplification curves for various values of the decay factor η_0, calculated with the "steady-state" analytical model, no transverse shear and

rotatory inertia.

Figure 19: Amplification factor for gages mounted near the flanges and the end. ⋄: experiments (a) Gage 11. (b) Gage 12. (c) Gage 13. (d) Gage 15. (e) Gage 16. (f) Gage 17. (g) Gage 18.

Figure 20: Measured pressure signals for a large cell size, detonation velocity 1267.4 m/s. (a) Pressure gage 1. (b) Pressure gage 2. (c) Pressure gage 3.

Figure 21: Amplification factor as a function of cell size for detonations at 1400 m/s. (a) Gage 3. (b) Gage 4. (c) Gage 5. (d) Gage 6. (e) Gage 7. (f) Gage 8. (g) Gage 9. (h) Gage 10.

Figure 22: Amplification factor as a function of cell size for detonations at 1268 m/s. (a) Gage 3. (b) Gage 4. (c) Gage 5. (d) Gage 6. (e) Gage 7. (f) Gage 8. (g) Gage 9. (h) Gage 10.

Figure B.1: Example of curve fit pressure history. □: exact, —: exponential decay approximation.

Figure 1:

pressure

p

$p_2 \, p$

p

distance

| stationary rocts | eansion ae | v_{cj} stationary reactants |

etonation
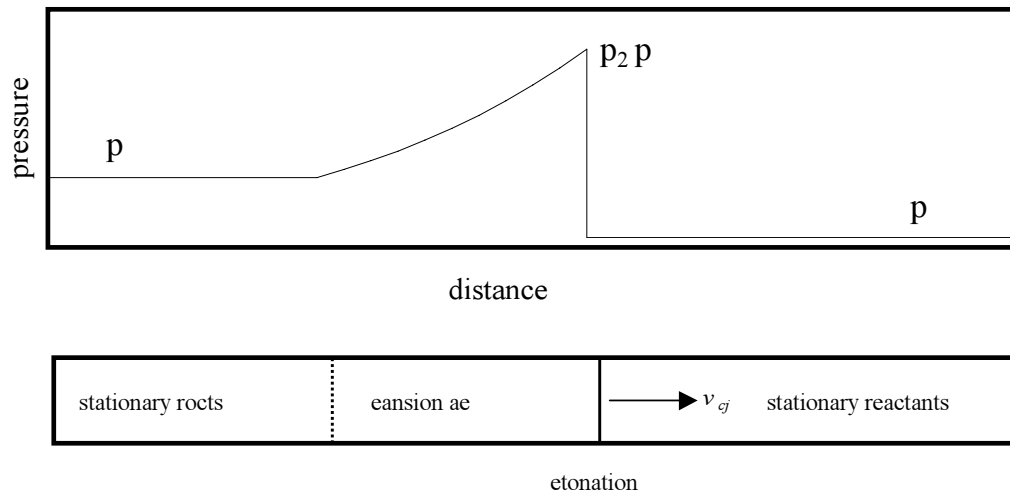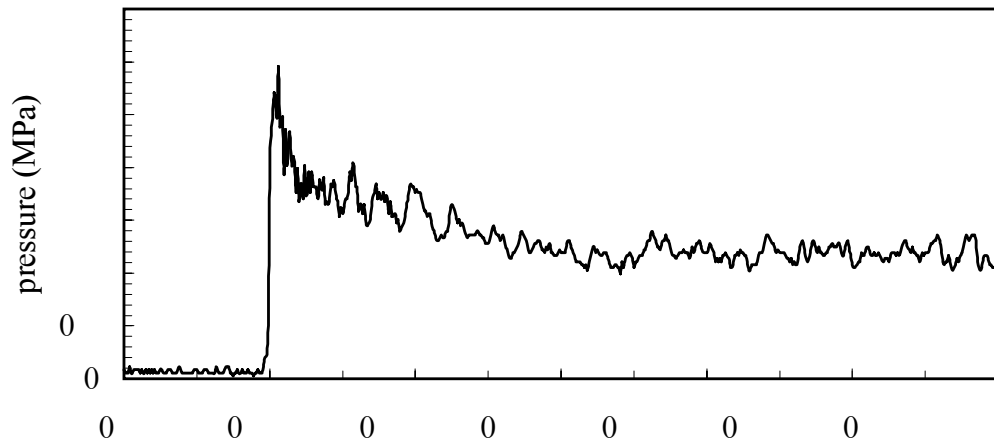
Figure 2:

(a)
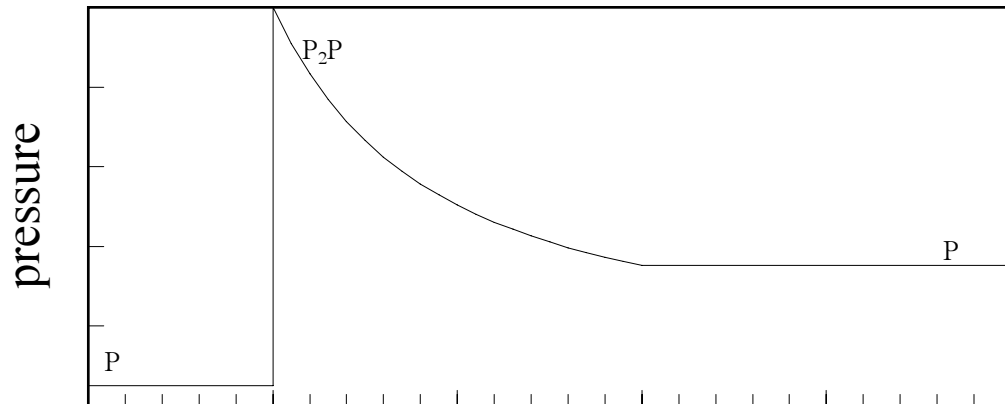
(b)
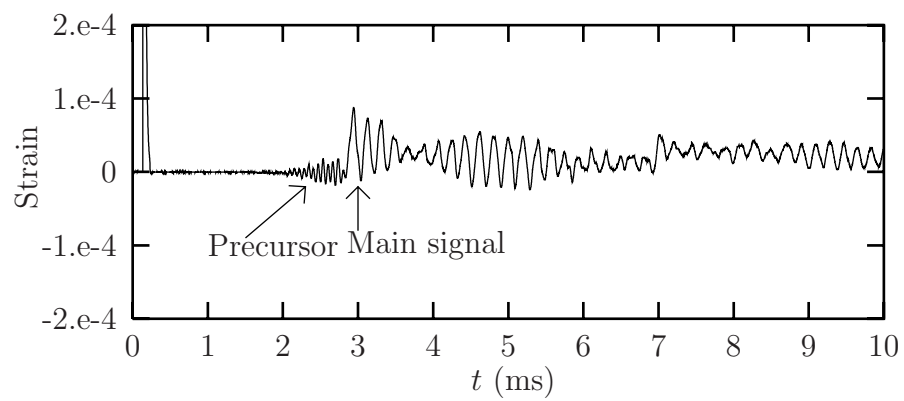
Figure 3:

Figure 4:

Figure 5:

Figure 6:

Exploding Wire
Holder

Oxy—Acetylene Delivery Tubes (Driver)

Glow plug ignitor

Transducer 1

Transducer 2

Transducer 3

Linear bearing blocks

Supporting I—beam
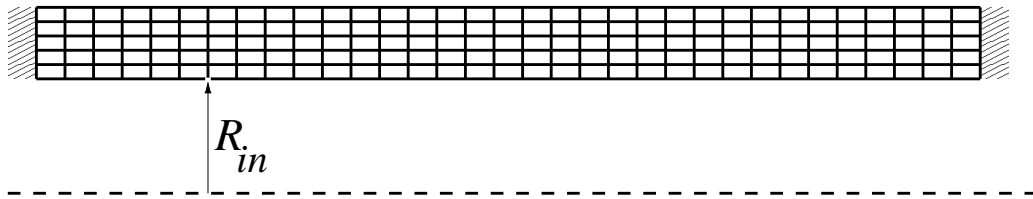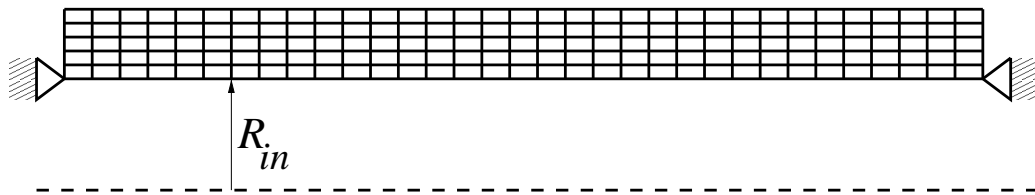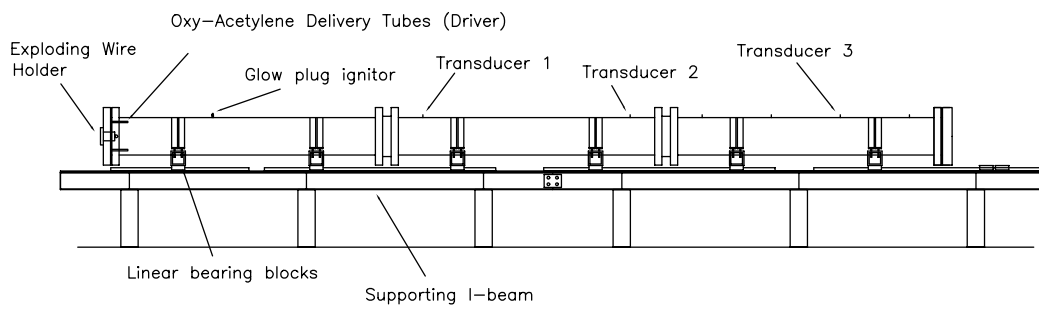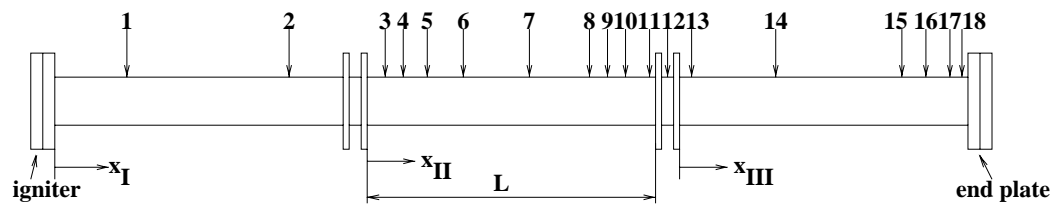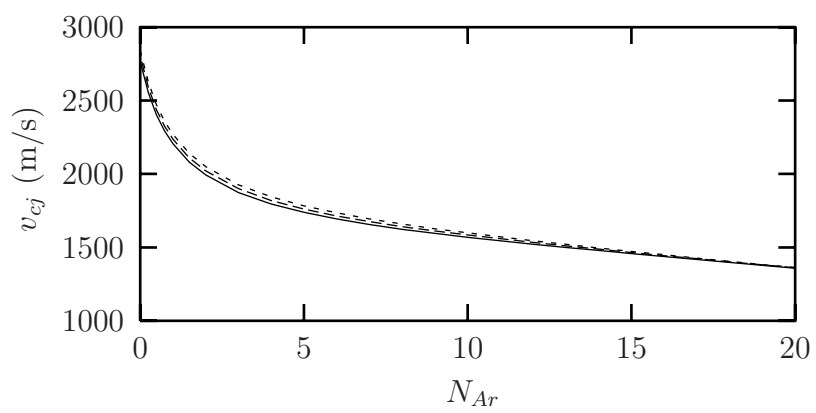
Figure 7:

(a)
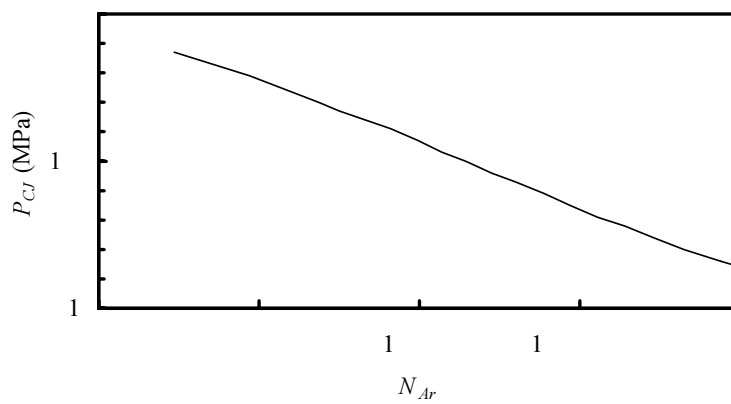
(b)

Figure 8:

Figure 9:
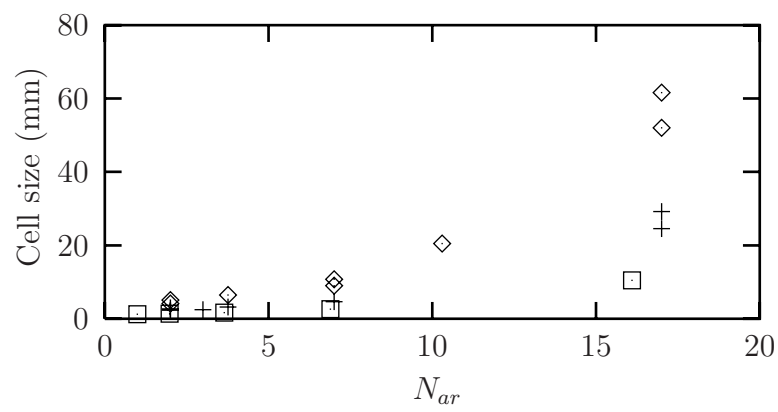
Figure 10:
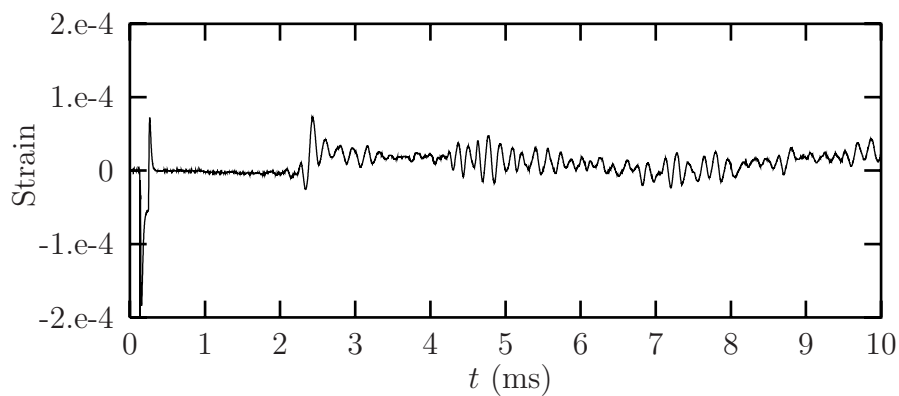
(a)
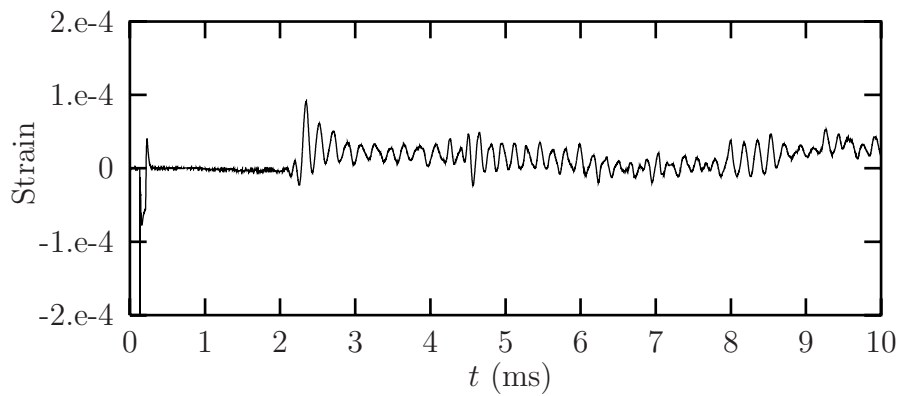
(b)
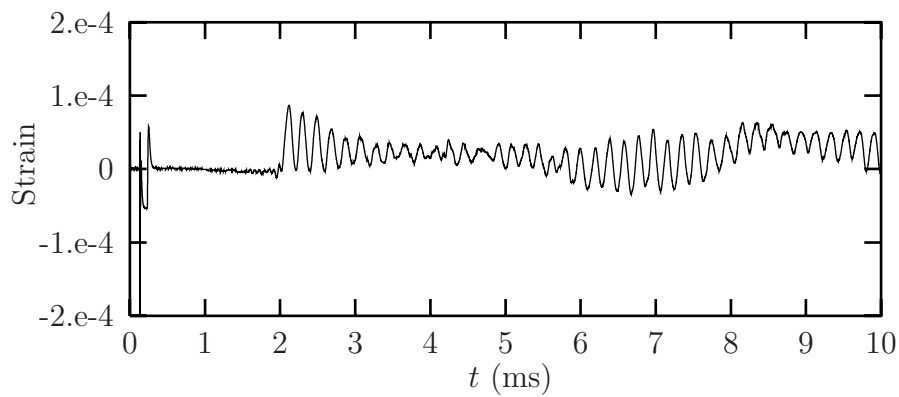
(c)

Figure 11:
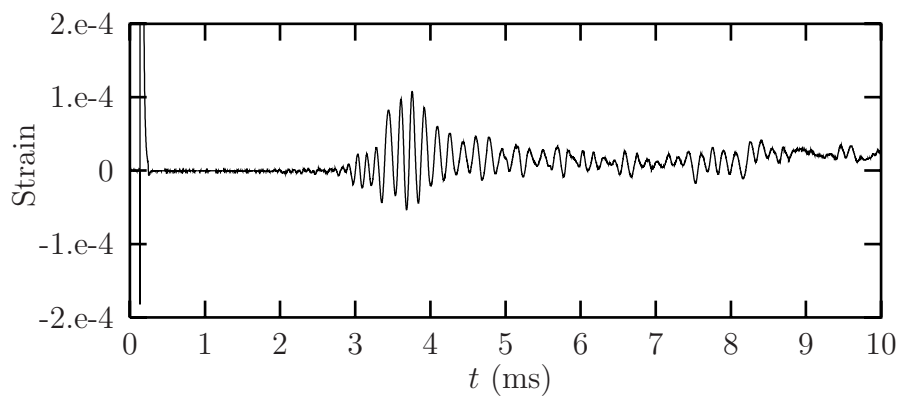
(a)
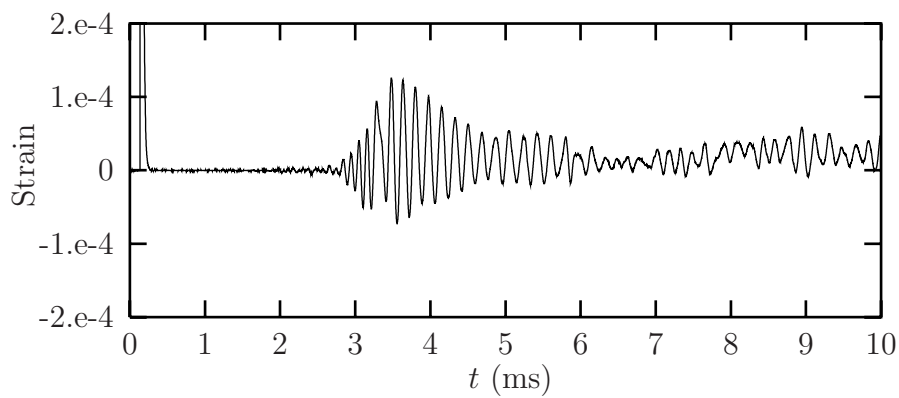
(b)
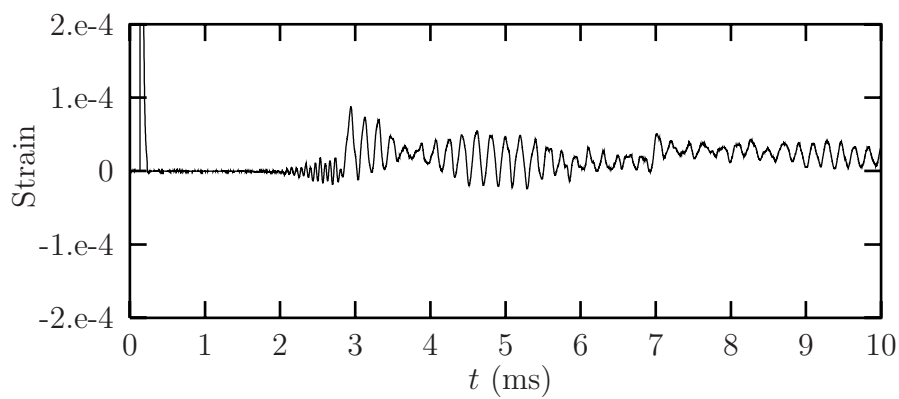
(c)

Figure 12:
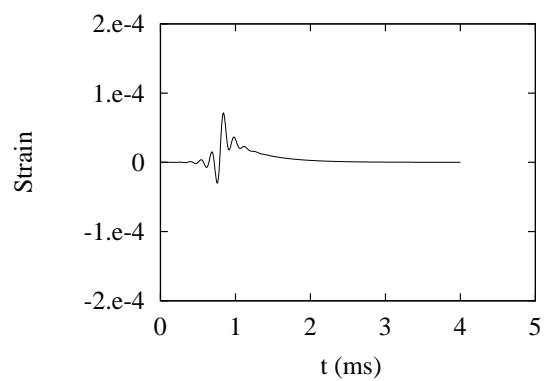
(a)
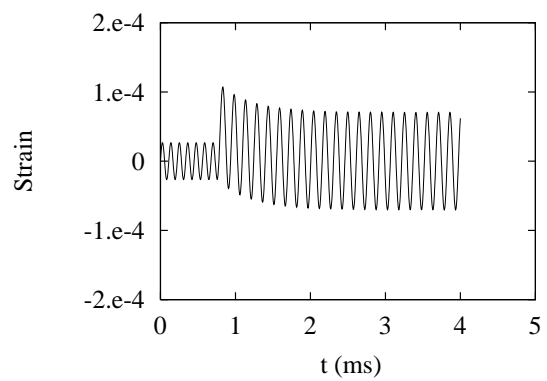
(b)
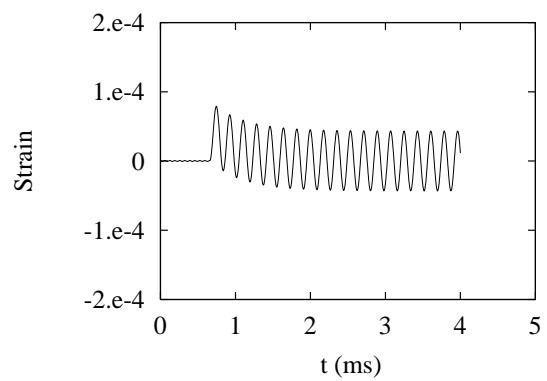
(c)

Figure 13:

(a)

(b)

(c)

(d)

(e)

(f)

Figure 14:

(a)

(b)

(c)

(d)

(e)

(f)

Figure 15:

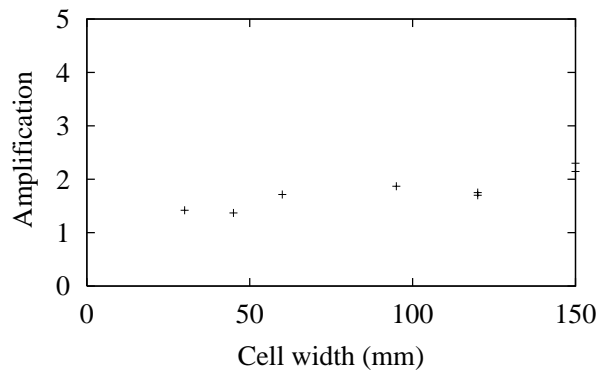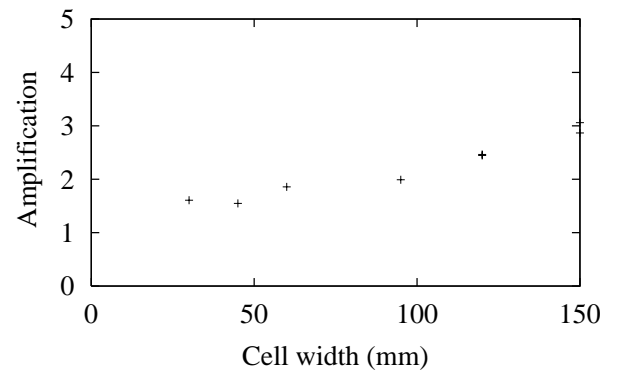(a)

(b)

(c)

(d)

(e)

Figure 16:

(a)

(b)

(c)

(d)
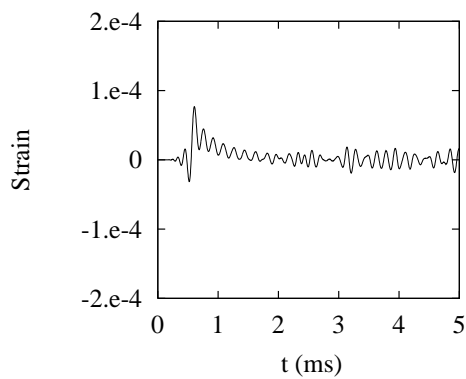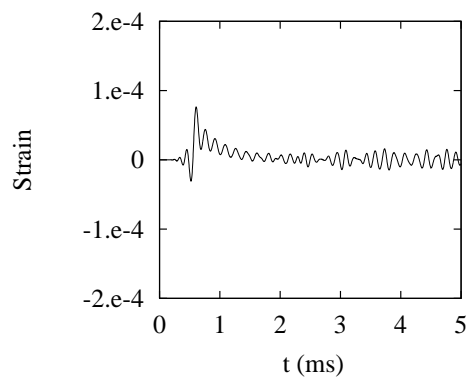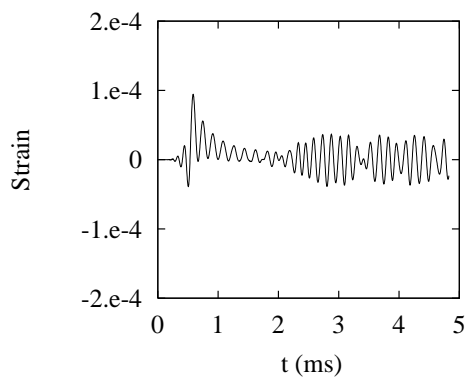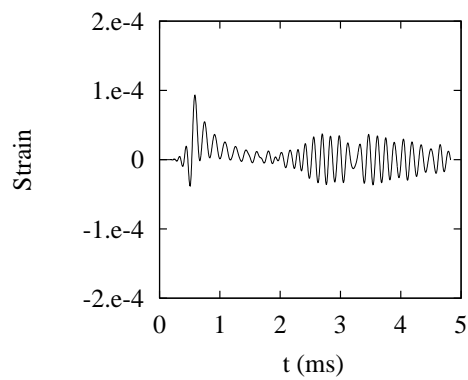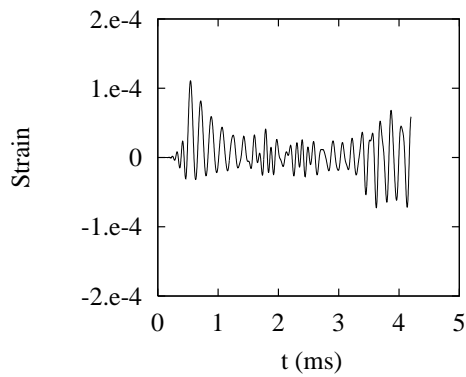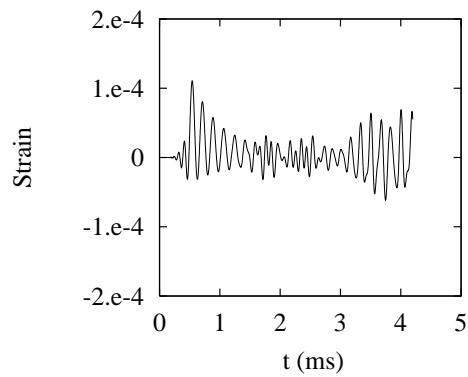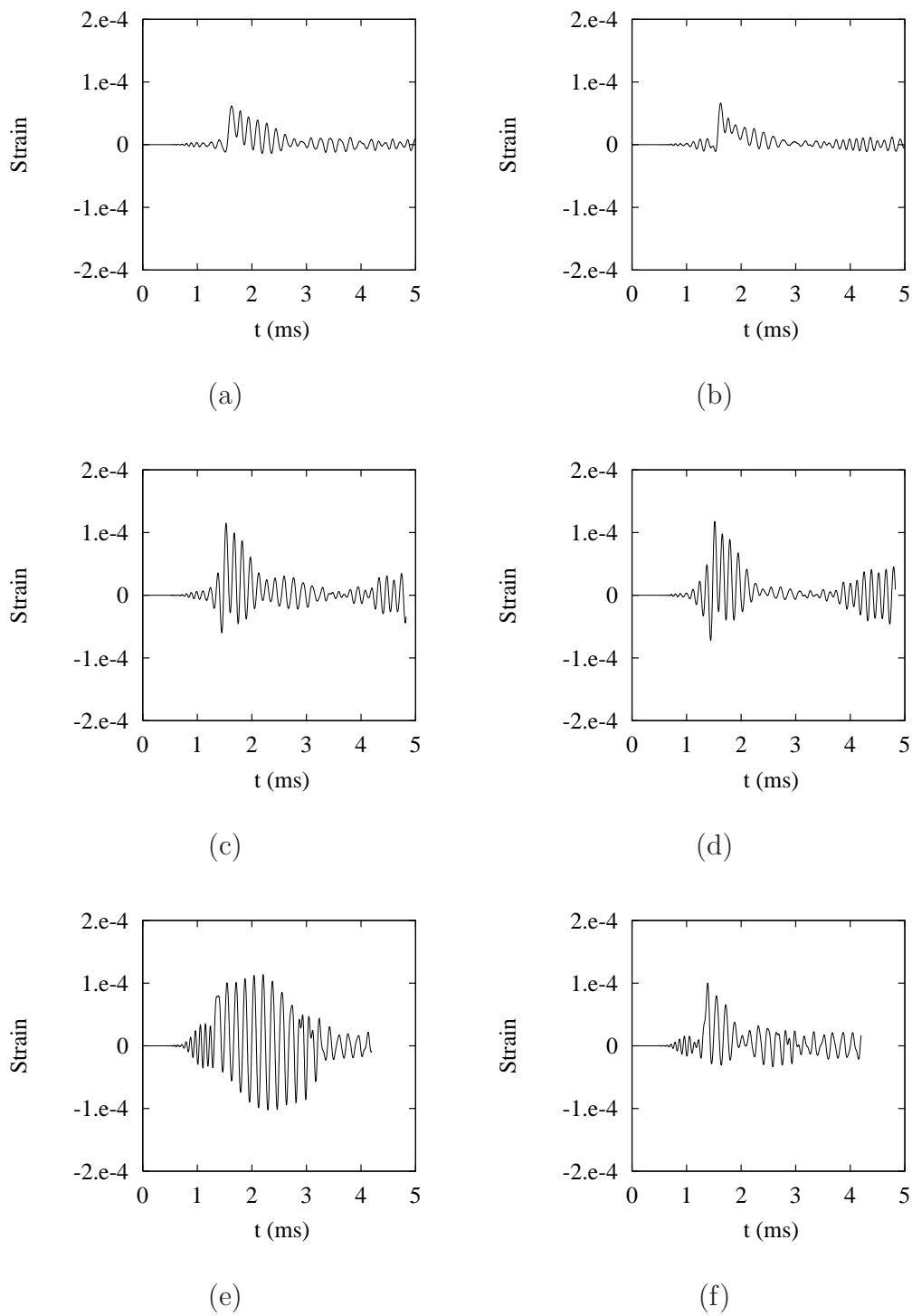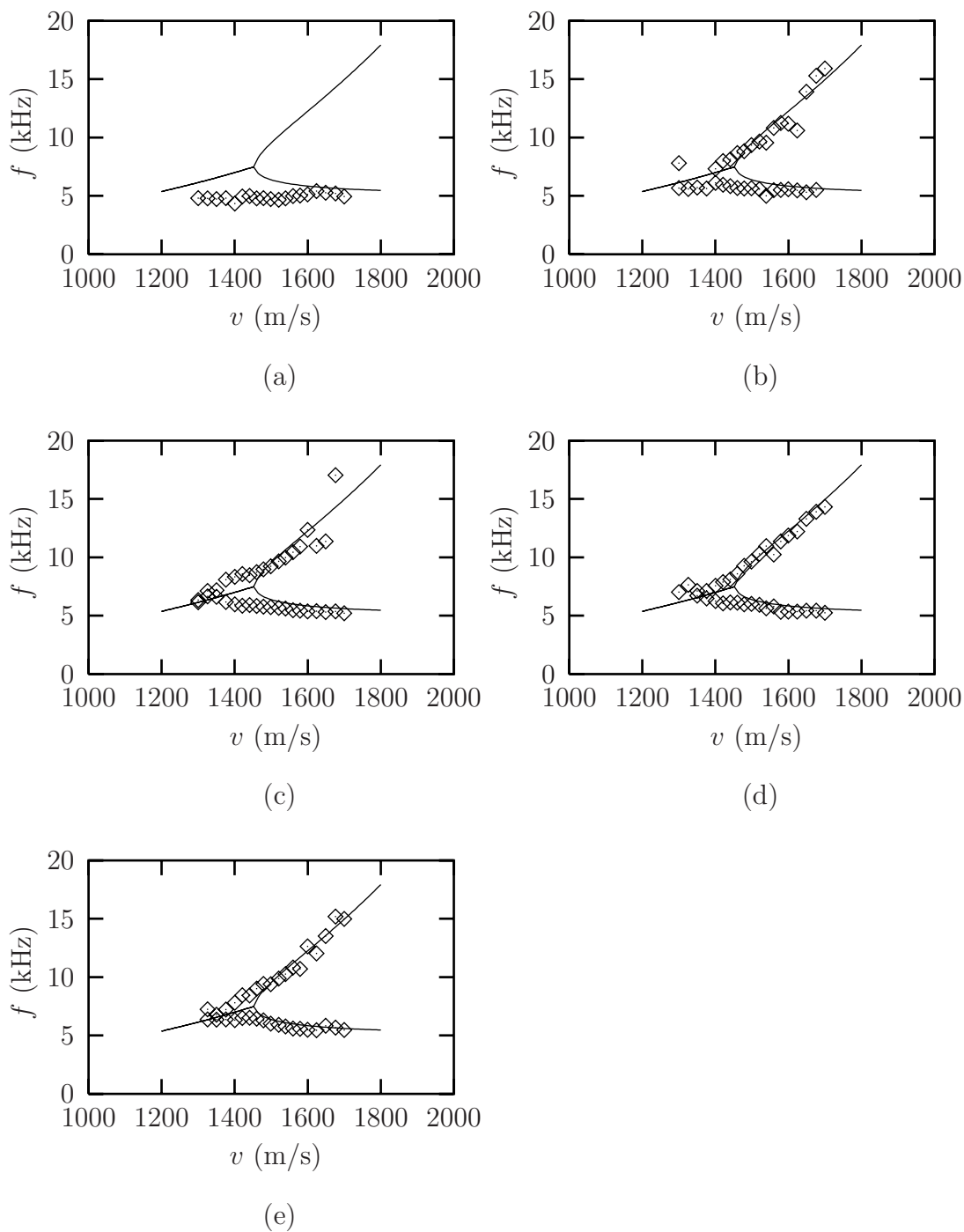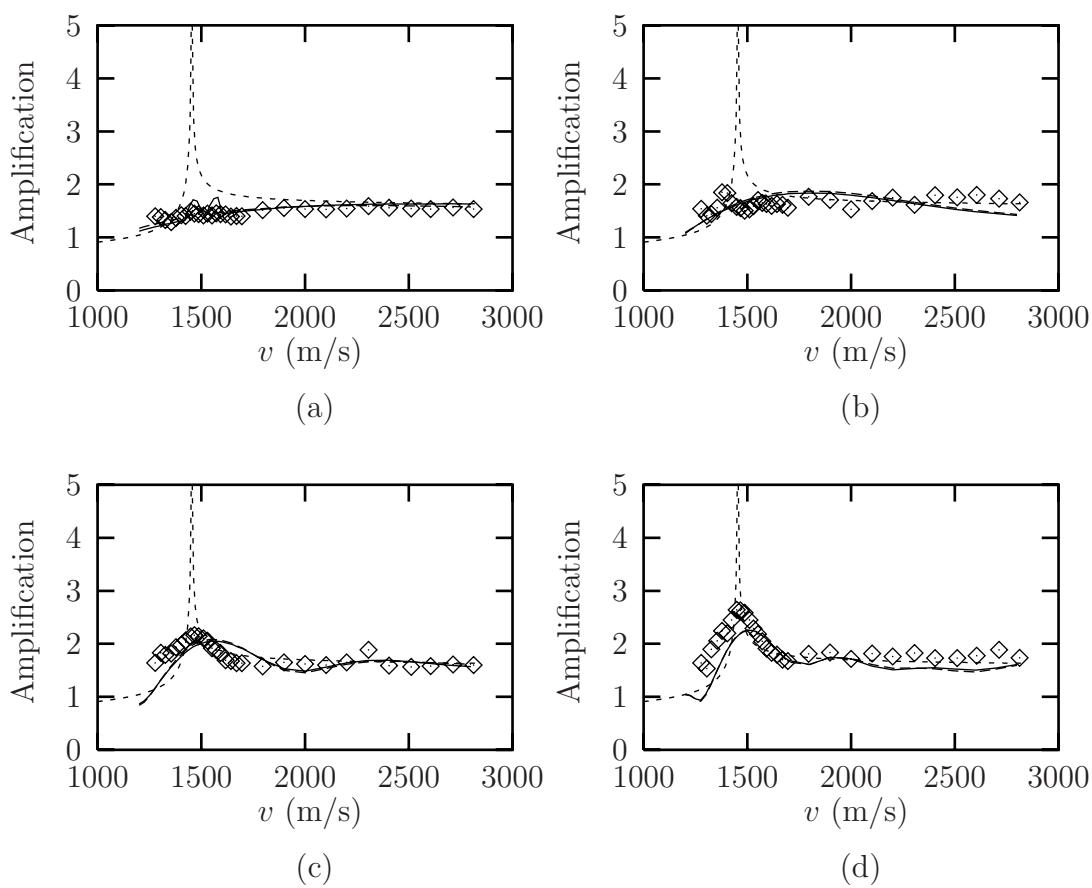
Figure 16: (continued)

(e)

(f)

(g)

(h)

Figure 17:

(a)

(b)

(c)

(d)
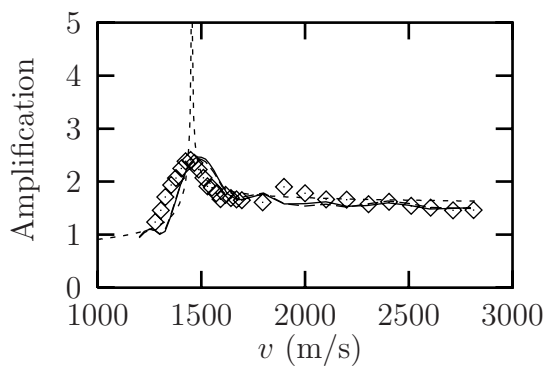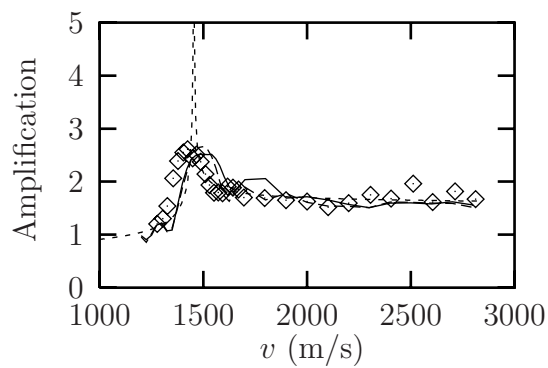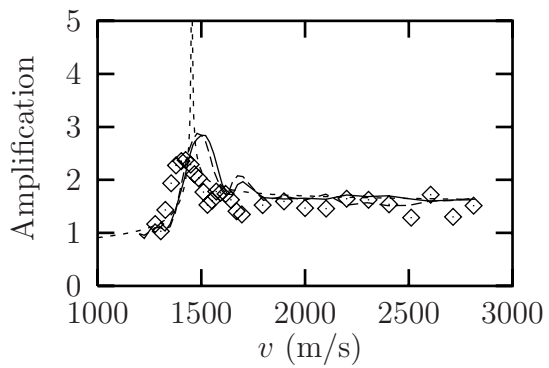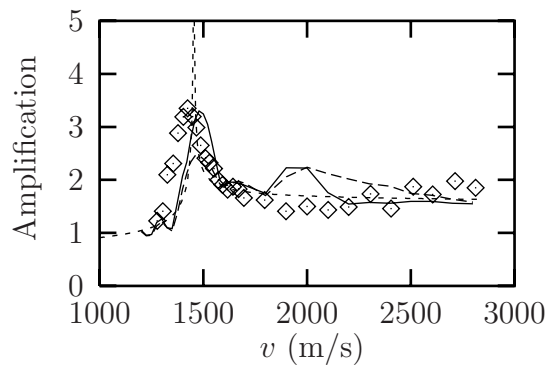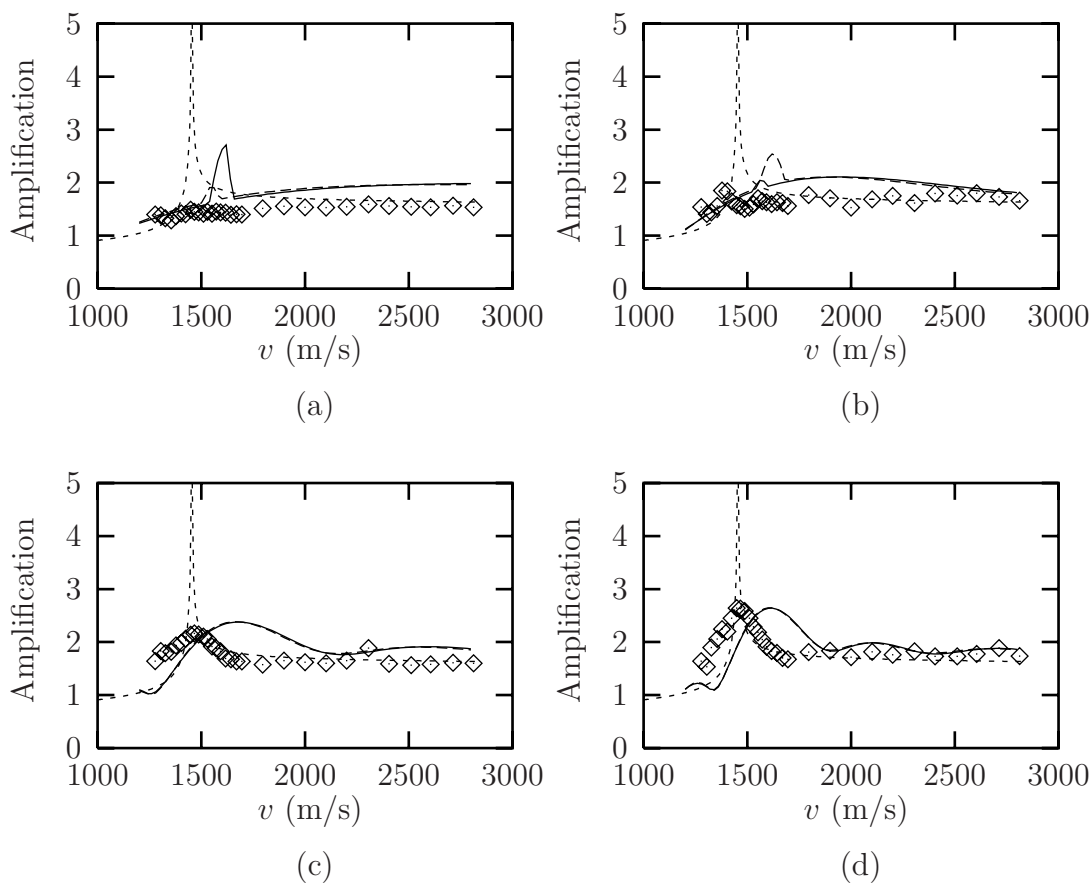
Figure 17: (continued)
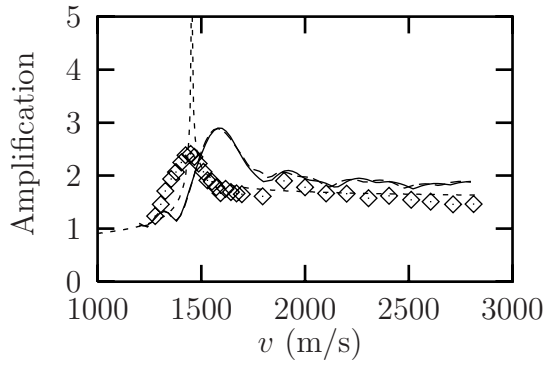
(e)
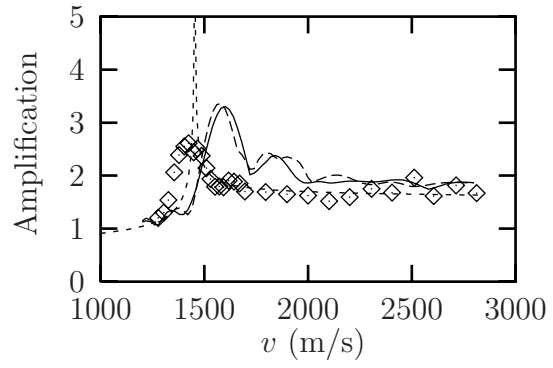
(f)
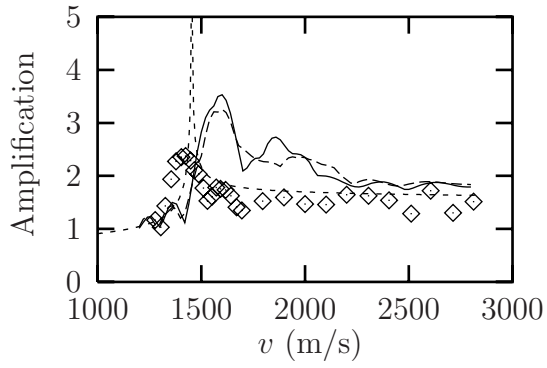
(g)
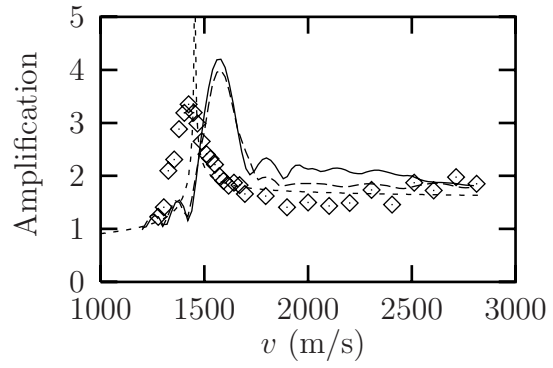
(h)

Figure 18:

Figure 19:

(a)

(b)

(c)
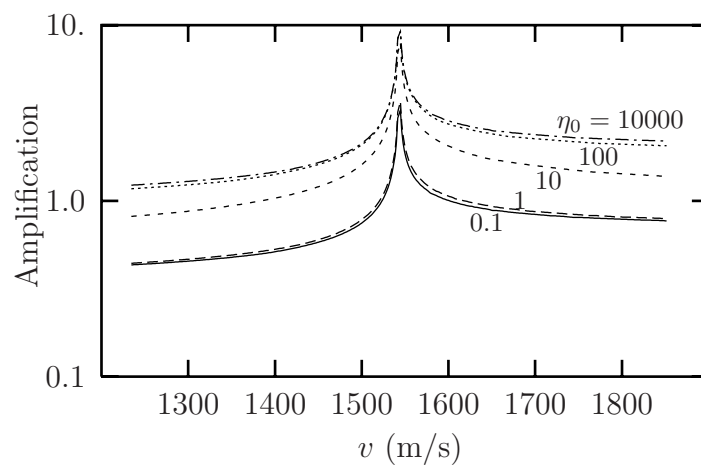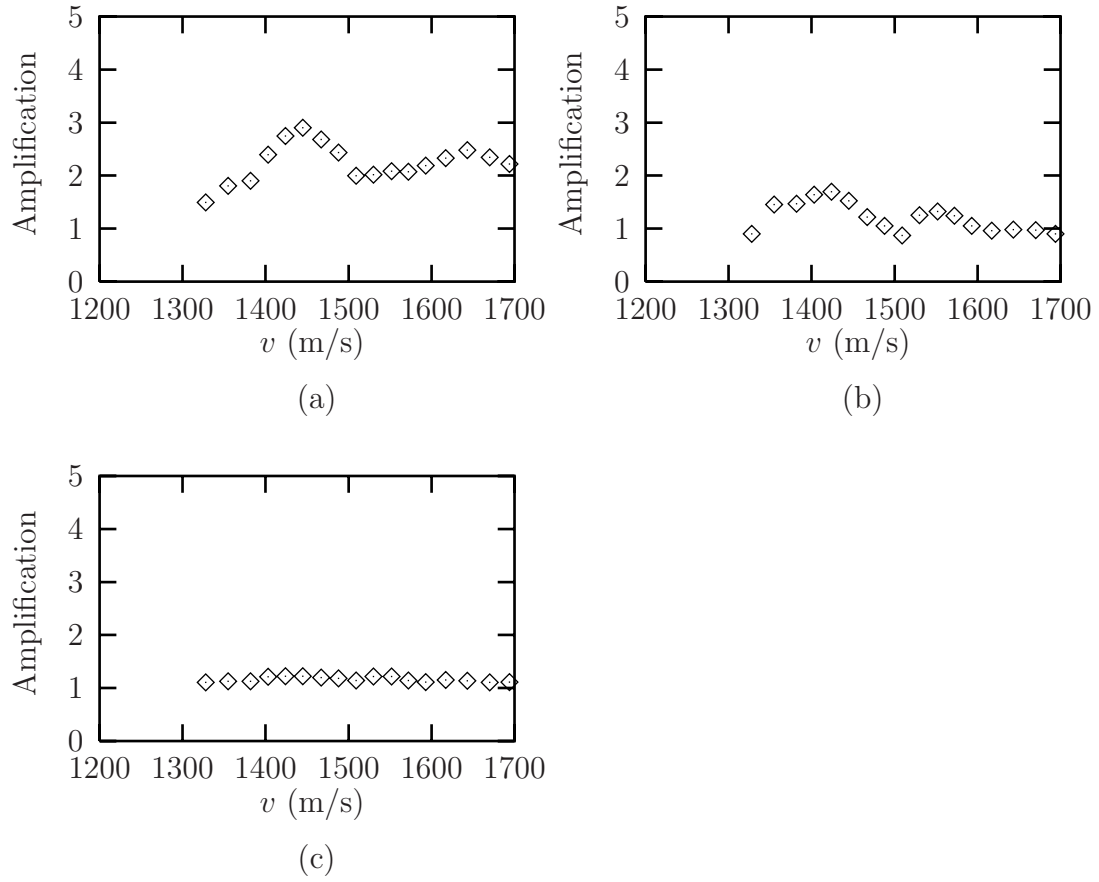
Figure 19: (continued)
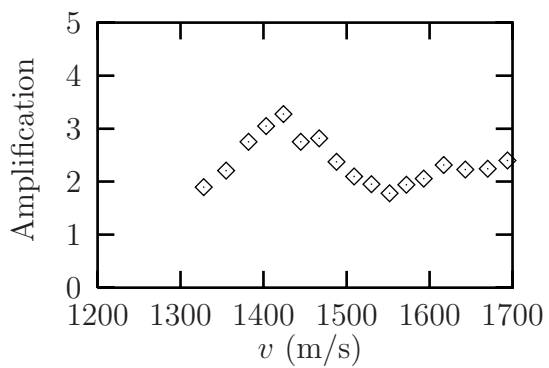
(d)
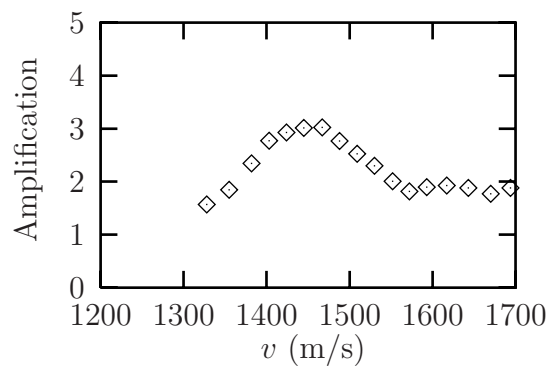
(e)
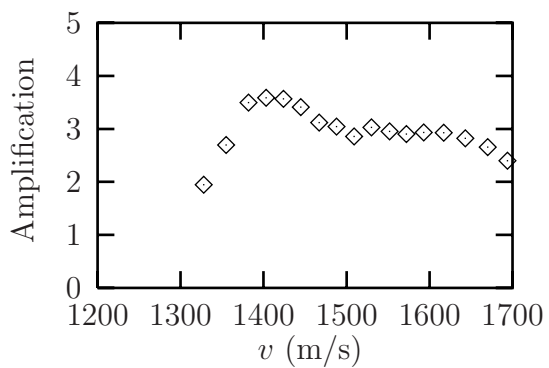
(f)
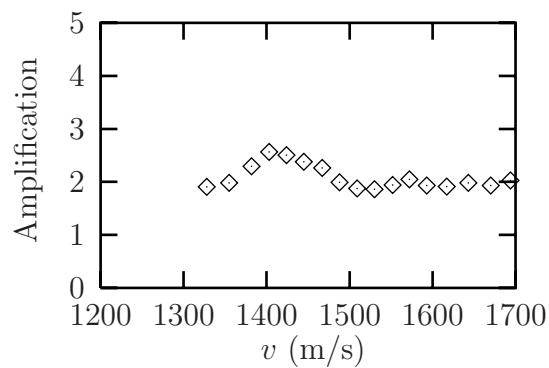
(g)

Figure 20:
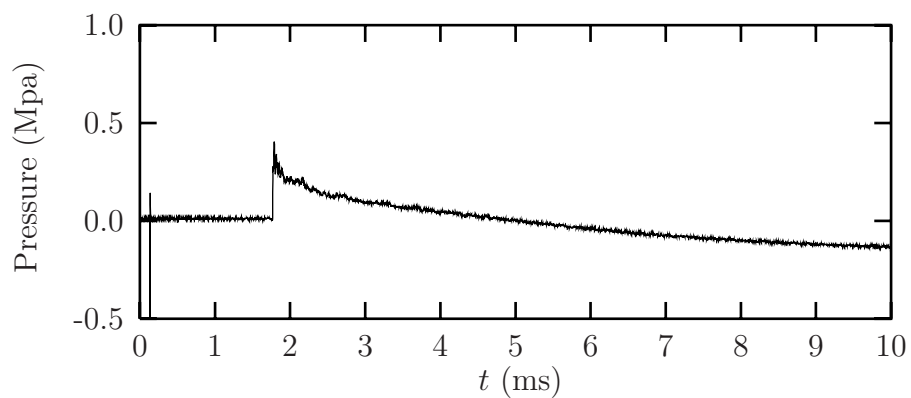
(a)
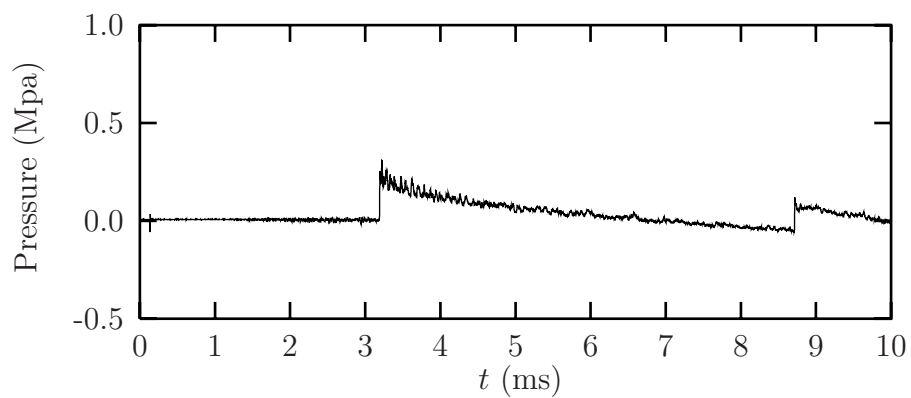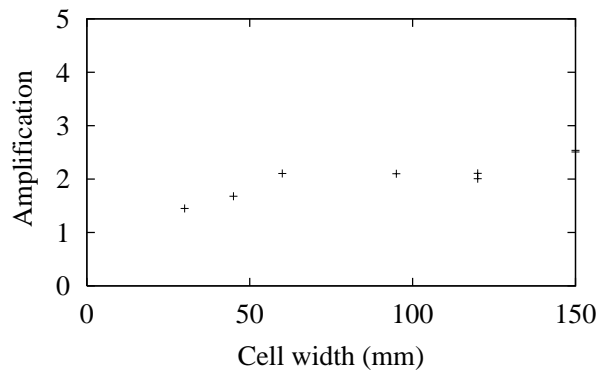
(b)
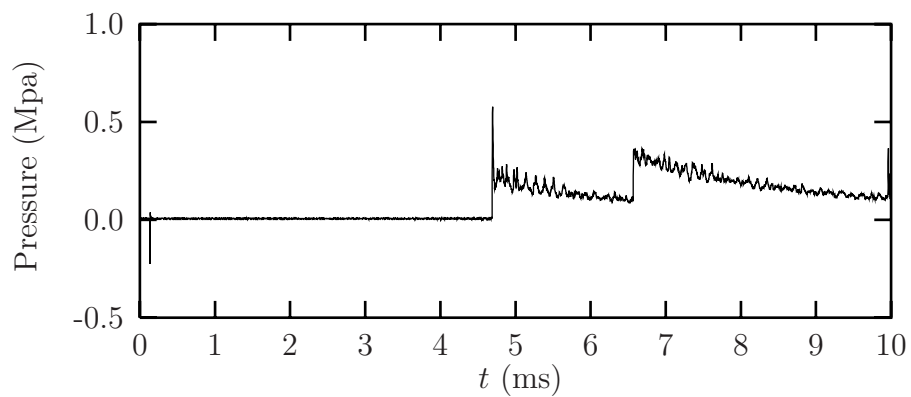
(c)

Figure 21:
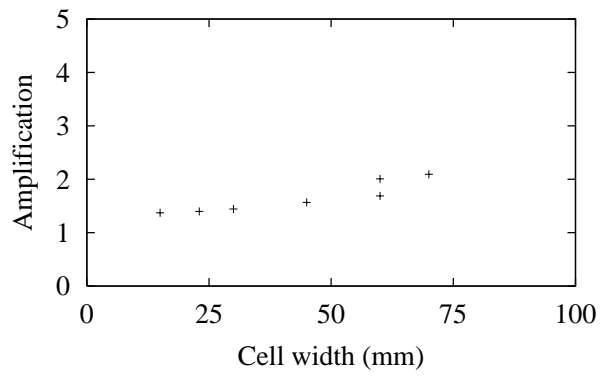
(a)
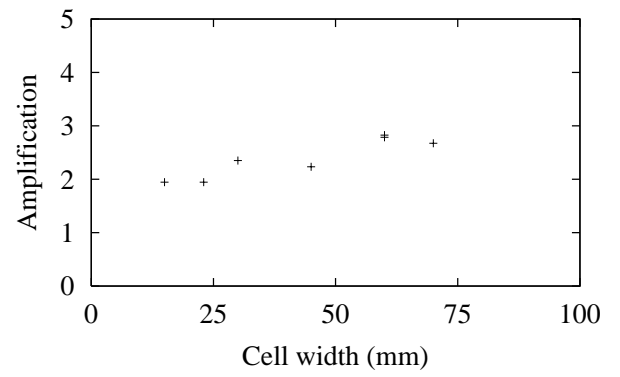
(b)
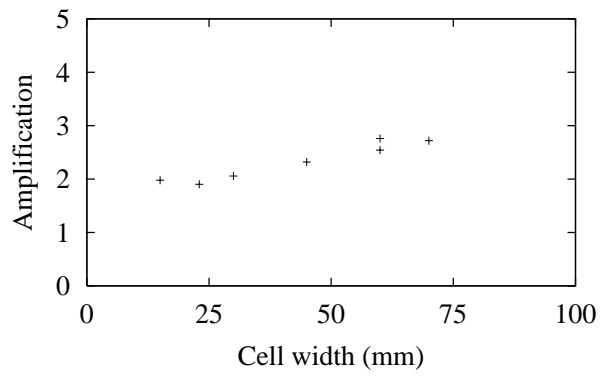
(c)
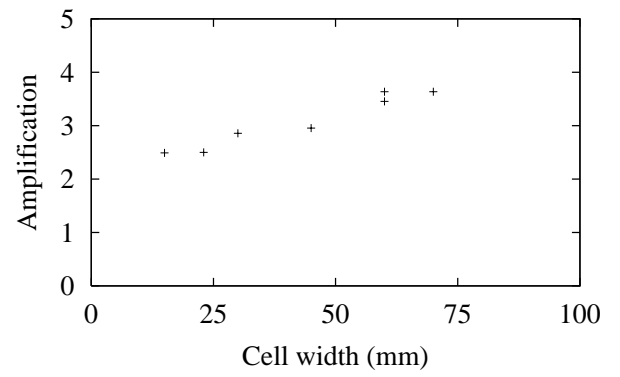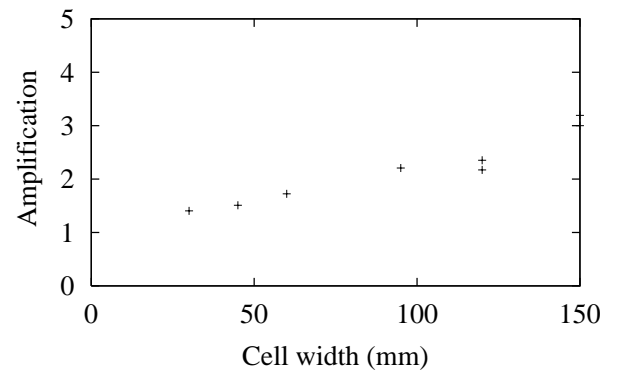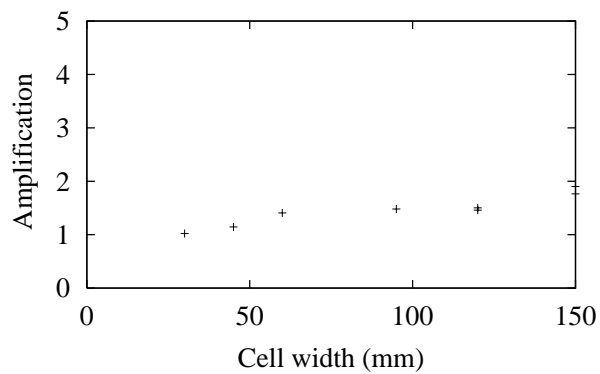
(d)

Figure 21: (continued)
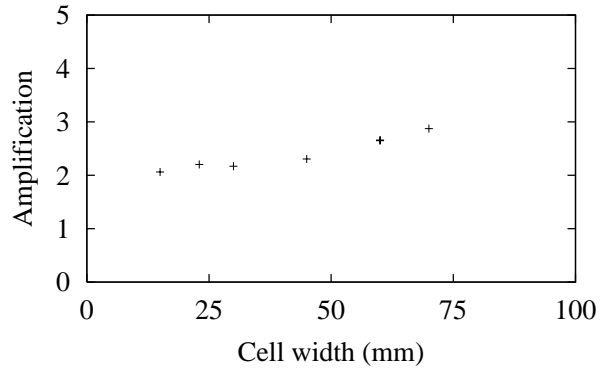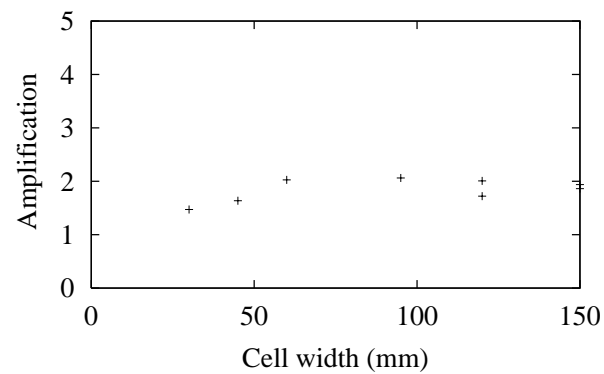

(e)
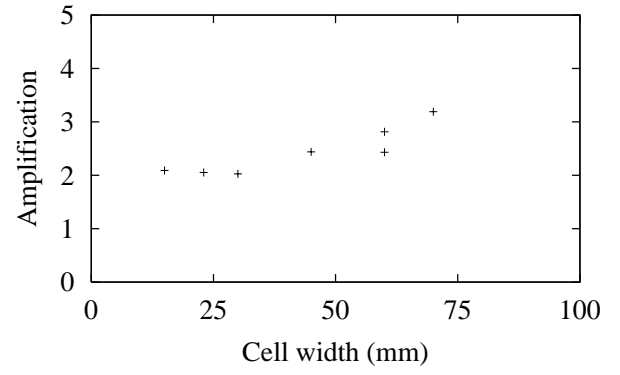
(f)
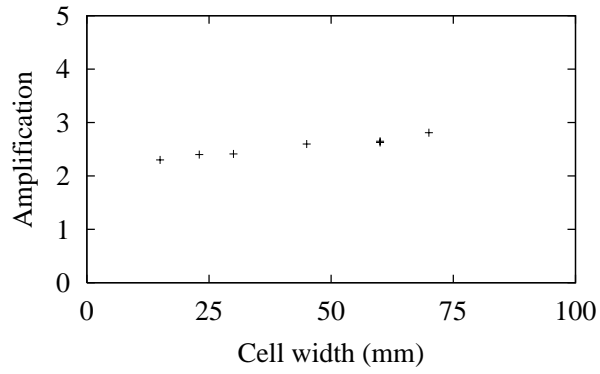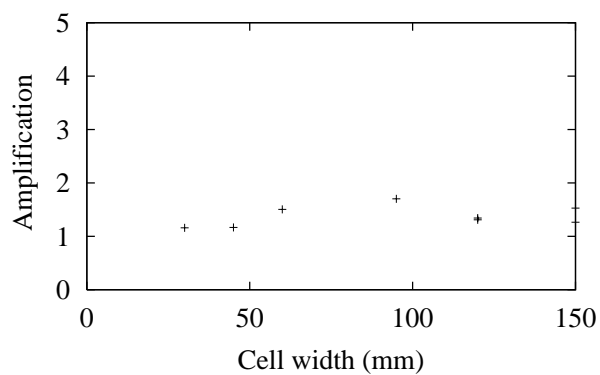

(g)
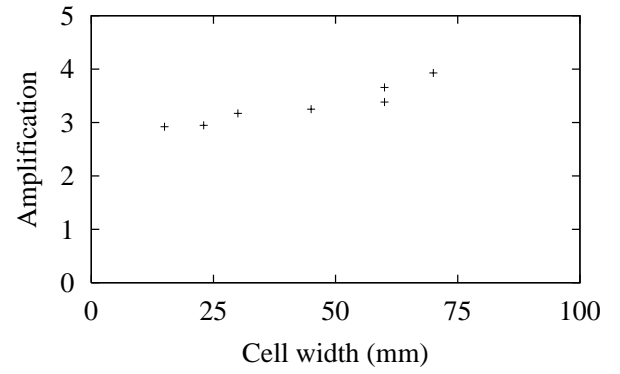
(h)

Figure 22:
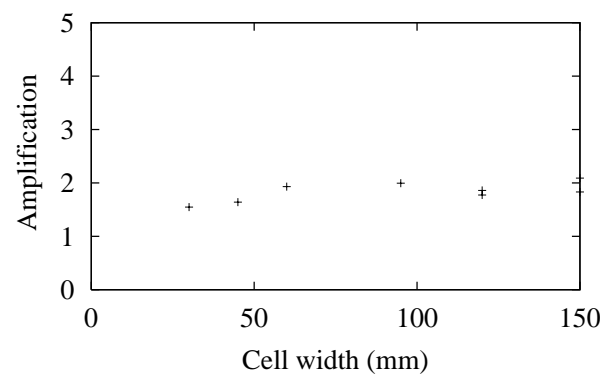

(a)

(b)

(c)

(d)

Figure 22: (continued)

(e)

(f)

(g)

(h)

Figure B.1:
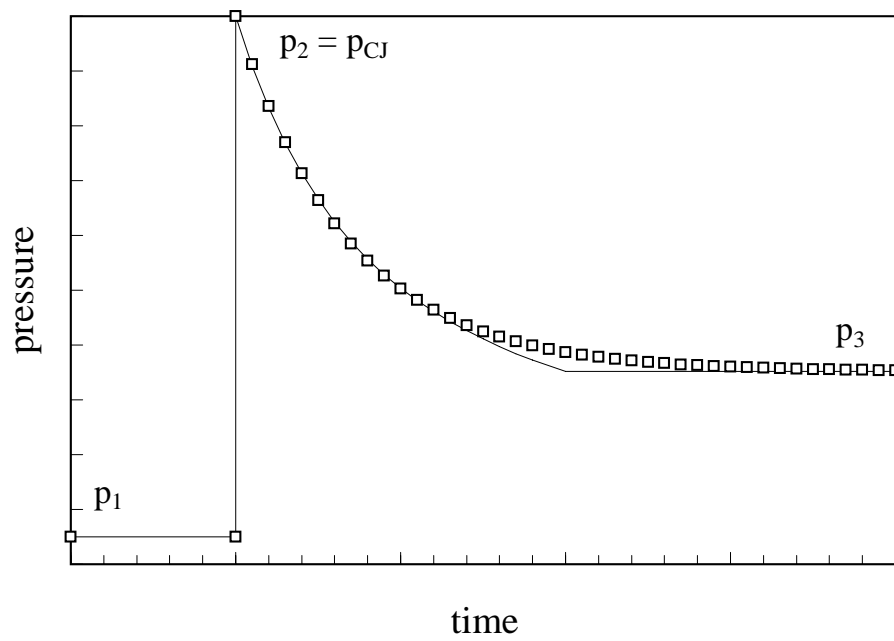
List of table captions

Table 1: Material properties and critical dimensions of the GALCIT 288 mm detonation tube.

Table 2: Locations of strain gages.

Table 3: Amplification factors for linearity shots at 1800 m/s.

Table 4: Amplification factors for linearity shots at 2000 m/s.

Table 1:

E	$=$	$193 \cdot 10^9$	N/m^2	ρ	$=$	$8 \cdot 10^3$	kg/m^3
ν	$=$	0.23		R_{in}	$=$	0.1397	m
R_{out}	$=$	0.1651	m	L	$=$	2.38	m

Table 2:

Gage	x (m)	$\frac{x}{L}$	Gage	x (m)	$\frac{x}{L}$
1	$x_I = 1.181$	0.496	10	$x_{II} = 2.195$	0.923
2	$x_I = 1.951$	0.820	11	$x_{II} = 2.273$	0.955
3	$x_{II} = 0.248$	0.104	12	middle	
4	$x_{II} = 0.433$	0.182	13	$x_{III} = 0.094$	0.039
5	$x_{II} = 0.790$	0.332	14	$x_{III} = 1.181$	0.496
6	$x_{II} = 1.181$	0.496	15	$x_{III} = 1.951$	0.820
7	$x_{II} = 1.567$	0.659	16	$x_{III} = 2.085$	0.876
8	$x_{II} = 1.951$	0.820	17	$x_{III} = 2.160$	0.908
9	$x_{II} = 2.085$	0.876	18	$x_{III} = 2.243$	0.943

Table 3:

p_{cj}	Amplification for gage					
(MPa)	1	2	6	8	14	15
0.43	1.927	1.733	2.042	1.935	1.882	2.849
0.88	2.051	1.760	1.850	2.008	1.871	2.629
1.33	2.133	2.159	1.833	1.882	1.825	2.875
1.79	2.012	1.959	1.816	1.751	1.800	2.911

Table 4:

p_{cj}	Amplification for gage					
(MPa)	1	2	6	8	14	15
0.45	1.749	1.501	1.765	1.552	1.752	2.137
0.91	1.501	1.439	1.693	1.461	1.703	2.091
1.39	1.617	1.421	1.655	1.487	1.722	2.235
1.87	1.543	1.385	1.643	1.467	1.703	2.167

List of Footnotes

1. The modes are written in this way because of numerical stability considerations.

2. **G**raduate **A**eronautical **L**aboratories,**C**alifornia **I**nstitute of **T**echnology

3. acetylene: C_2H_2

4. The large spike that is present in all strain signals at $t = 0$ is caused by the discharge of the capacitor.